

Transition from quasi-elastic to deep-inelastic reactions in the $^{48}\text{Ti} + ^{208}\text{Pb}$ system

K. E. Rehm, A. M. van den Berg,* J. J. Kolata,[†] D. G. Kovar, W. Kutschera, G. Rosner,[‡]
G. S. F. Stephans,[§] and J. L. Yntema

Argonne National Laboratory, Argonne, Illinois 60439

(Received 14 December 1987)

Transfer reaction cross sections for the systems $^{46,48,50}\text{Ti} + ^{208}\text{Pb}$ at $E_{\text{c.m.}} = 243$ MeV have been measured with single mass and charge resolution using a magnetic spectrograph and a gas-filled focal-plane detector. The angle and excitation energy ranges studied in this experiment covered both quasi-elastic and deep-inelastic processes. The total reaction cross sections are dominated by transfer reactions with neutron transfer being the strongest transfer mode. Wilczyński plots for individual reaction channels have been generated showing a gradual transition from quasi-elastic reactions to deep-inelastic processes. While macroscopic models cannot explain the element distributions observed in this experiment, a simple model based on a random walk in the N - Z plane gives good agreement for the reaction strength and the measured energy spectra.

I. INTRODUCTION

Heavy-ion induced transfer reactions have been studied during the past few years over a large range of energies and with various projectile-target combinations. As a result of these investigations two reaction types have emerged which are usually summarized under the titles "quasi-elastic" and "deep-inelastic" reactions. While no clear separation between the two mechanisms seems to exist, it has been observed that quasi-elastic processes (inelastic scattering to low-lying levels in projectile and target, few nucleon transfer) are more prevalent in reactions induced by lighter projectiles (e.g., ^{16}O).^{1,2} Reactions induced by heavier projectiles (e.g., Kr, Xe) are found instead to be dominated by processes in which large amounts of kinetic energy are dissipated into internal excitation energies of the two emerging fragments³ (deep-inelastic scattering).

Only a few studies have addressed the question of whether these two reaction types are two separate mechanisms, or if there is a continuous transition from quasi-elastic to deep-inelastic scattering. The main reason for the lack of information in this transitional regime is the experimental difficulty in obtaining data with good mass, charge, and Q -value resolution for the heavier projectiles, where both mechanisms coexist. It is only recently that data with heavier projectiles have become available.⁴⁻¹² In these studies it is observed that, even for heavy projectiles (Ti, Fe, Ni, Kr), quasi-elastic transfer reactions (particularly neutron transfer) contribute substantially to the total reaction cross section especially at incident energies not too high above the Coulomb barrier.

In the present study we have investigated the $^{46,48,50}\text{Ti} + ^{208}\text{Pb}$ systems at energies which are about 25% above the Coulomb barrier in the entrance channel. It was our aim to achieve single mass and charge resolution over the full energy range from quasi-elastic to deep inelastic reactions, in order to study the transition between these two processes in detail. Data taken from $\theta_{\text{lab}} = 20-80^\circ$ allowed the production of Wilczyński

plots¹³ for individual reaction channels in the system $^{48}\text{Ti} + ^{208}\text{Pb}$. Cross sections for the three isotopes $^{46,48,50}\text{Ti}$ were measured in an attempt to answer the question as to whether the strong quasi-elastic neutron transfer processes, first observed in Ref. 5, can be influenced by inelastic scattering. ^{46}Ti has the highest $B(E2)$ value to the first excited 2^+ state of all projectiles available in the f - p shell, while the corresponding value for ^{50}Ti is smaller by a factor of about 4.

Details of the experimental setup are given in Sec. II, while experimental results are summarized in Sec. III. Section IV contains a discussion of these results within quasi-elastic and deep-inelastic models and also discusses the transition between the two processes within the framework of a random-walk description. Section V summarizes the main results of this investigation.

II. EXPERIMENTAL DETAILS

The measurements were performed at the Argonne National Laboratory ATLAS facility. The Ti beams were produced in an inverted sputter source¹⁴ using natural Ti samples loaded with hydrogen. Details about the source and the sample preparation are given elsewhere.¹⁵ TiH_3^- molecules were extracted from the source, accelerated in the FN tandem, and stripped to Ti^{9+} ions in the terminal. After a second stripper foil in front of the 90° analyzing magnet, Ti^{17+} ions were accelerated in the superconducting linac to 298, 300, and 302 MeV for $^{46,48,50}\text{Ti}$, respectively. Beam currents were measured in a Faraday cup located in the scattering chamber. A current of about 2 pA was achieved for ^{48}Ti . For the lower abundance isotopes ^{50}Ti and ^{46}Ti smaller currents of approximately 0.2–0.3 pA were obtained. The targets consisted of ^{208}Pb ($200 \mu\text{g}/\text{cm}^2$) evaporated onto $15 \mu\text{g}/\text{cm}^2$ carbon backings.

The outgoing particles were momentum analyzed in the Enge split-pole spectrograph and detected in the focal plane with a position-sensitive ionization chamber.¹⁶ The large dynamic range of the split-pole spectrograph en-

abled six charge states of the outgoing particles, representing more than 90% of the total charge state distribution, to be measured simultaneously in the focal plane detector.

Particle identification was achieved by measuring total energy E_{total} , energy loss ΔE , and the distance along the focal plane (related to the magnetic rigidity $B\rho$) in the position-sensitive ionization chamber. Figure 1(a) shows as an example the nuclear charge identification obtained from the ΔE - E_{total} plot for the reaction $^{48}\text{Ti} + ^{208}\text{Pb}$ at $E_{\text{lab}} = 300$ MeV and $\theta_{\text{lab}} = 55^\circ$. The ΔE signal has been corrected, using an additional angle measurement, for the different path lengths in the ΔE region of the ionization chamber which originate from the different trajectories through the magnet at a solid angle of 1 msr. Figure 1(b) shows a scatter plot of E_{total} versus $B\rho$ for particles with

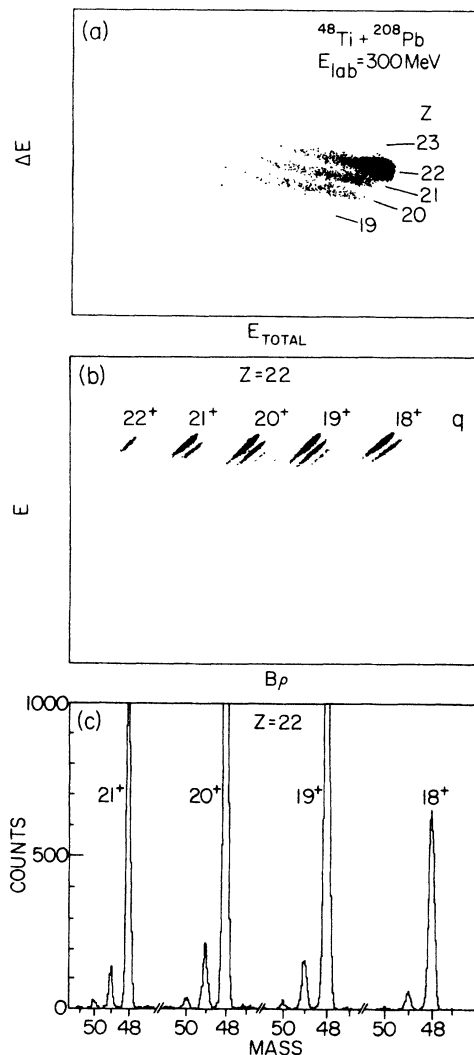


FIG. 1. (a) ΔE - E_{total} scatterplot obtained in the reaction $^{48}\text{Ti} + ^{208}\text{Pb}$ at $E_{\text{lab}} = 300$ MeV and $\theta_{\text{lab}} = 55^\circ$. (b) E_{total} - $B\rho$ scatter plot for particles with $Z=22$ from the reaction $^{48}\text{Ti} + ^{208}\text{Pb}$ at $E_{\text{lab}} = 300$ MeV and $\theta_{\text{lab}} = 55^\circ$. (c) Linearized mass spectrum for the four strongest charge states in the reaction $^{48}\text{Ti} + ^{208}\text{Pb}$.

$Z=22$ from the same reaction. The individual mass lines, clearly visible in this plot, can be linearized and then projected into a mass spectrum [see Fig. 1(c)]. The same procedure can be applied to the other elements, and some results for the reaction channels with $18 \leq Z \leq 23$ are shown in Fig. 2. The range of useful data was limited to $16 \leq Z \leq 24$. Outside of this range, the gas pressure in the ionization chamber was either too high (for $Z > 24$) or too low (for $Z < 16$) in order to yield good particle identification.

The energy resolution obtained in this experiment was about 3 MeV, primarily determined by the energy strag-

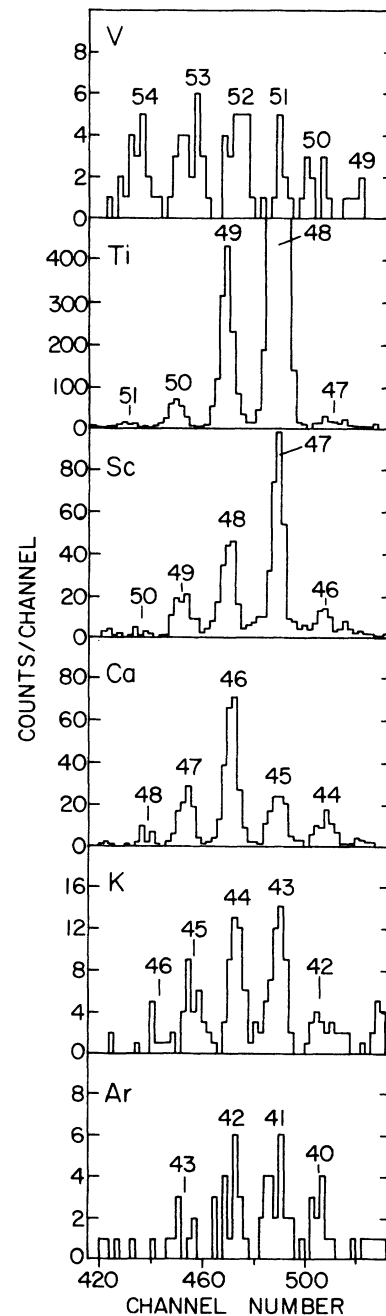


FIG. 2. Mass spectra for outgoing particles with $18 \leq Z \leq 23$ from the reaction $^{48}\text{Ti} + ^{208}\text{Pb}$ at $E_{\text{lab}} = 300$ MeV and $\theta_{\text{lab}} = 55^\circ$.

gling in the $200 \mu\text{g}/\text{cm}^2$ target. Therefore, transitions to individual states could not be resolved and only energy-integrated cross sections and centroids of the energy distributions will be discussed in the following. Figure 3 shows some energy spectra for the strongest channels in the reaction $^{48}\text{Ti} + ^{208}\text{Pb}$. While the $(^{48}\text{Ti}, ^{49}\text{Ti})$, $(^{48}\text{Ti}, ^{50}\text{Ti})$, and $(^{48}\text{Ti}, ^{47}\text{Sc})$ spectra are dominated by quasi-elastic peaks centered at Q values above -20 MeV, a more negative average Q value is observed for the more complicated transfer reactions $(^{48}\text{Ti}, ^{46}\text{Ca})$ and $(^{48}\text{Ti}, ^{48}\text{Sc})$.

Angular distributions were measured in the range $20^\circ \leq \theta_{\text{lab}} \leq 80^\circ$. Two monitor detectors mounted at $\theta_{\text{lab}} = \pm 13^\circ$ served to establish the relative normalization for the individual runs. Absolute cross sections were obtained by normalizing the ^{48}Ti elastic yields at the most-forward angles ($\theta = 20^\circ, 25^\circ$) to the corresponding Rutherford cross sections. For the strong channels with $20 \leq Z \leq 22$, 90% or more of the total charge state distribution was measured with a single magnetic-field setting. Therefore an extrapolation of the missing charge states did not pose a problem. The uncertainty in the absolute cross sections is estimated to be about 10%. For elements where only incomplete charge state distributions could be measured ($Z \leq 19$ and $Z \geq 23$), the missing charge state contributions were estimated by using a parametrization of the charge state distributions, with parameters obtained from an extrapolation of the results for $20 \leq Z \leq 22$. It should be noted that the energy dependence of the measured charge state distributions is in

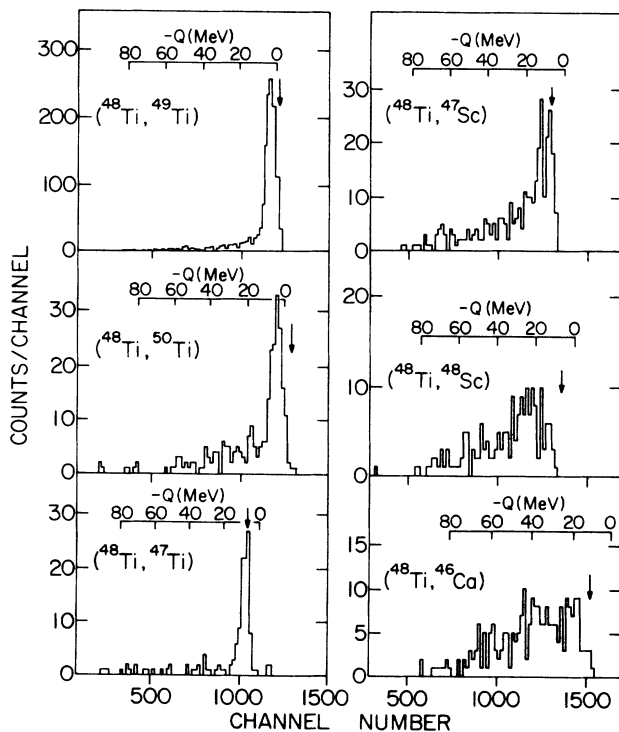


FIG. 3. $B\rho$ spectra (converted to a Q -value scale) for the strongest charge state component for several transfer reactions in the system $^{48}\text{Ti} + ^{208}\text{Pb}$ at $E_{\text{lab}} = 300$ MeV and $\theta_{\text{lab}} = 55^\circ$. The arrows indicate the corresponding ground-state Q value.

quite good agreement with the theoretical predictions of Ref. 17.

As mentioned above, the large dynamic range of the spectrograph allowed the study of quasi-elastic and deep-inelastic reactions with the same magnetic-field setting. As an example, Fig. 4 shows energy spectra for all outgoing particles from the $^{48}\text{Ti} + ^{208}\text{Pb}$ reaction measured at different scattering angles. A component associated with large negative Q values, up to -100 MeV, is observed, especially at forward angles. Since the incident energy is only about 45 MeV above the Coulomb barrier in the entrance channel, strongly deformed configurations must be associated with these large negative Q -value events.

III. EXPERIMENTAL RESULTS

A. Elastic and inelastic scattering

Figure 5 shows angular distributions for "elastic" scattering of $^{46,48,50}\text{Ti}$ on ^{208}Pb at $E_{\text{lab}} = 298, 300, 302$ MeV, respectively. In these cross sections, inelastic excitations up to 3 MeV excitation energy are included. The angular distributions for the three different projectiles have the same quarter-point angle ($\theta_{1/4} = 79^\circ$) and differ

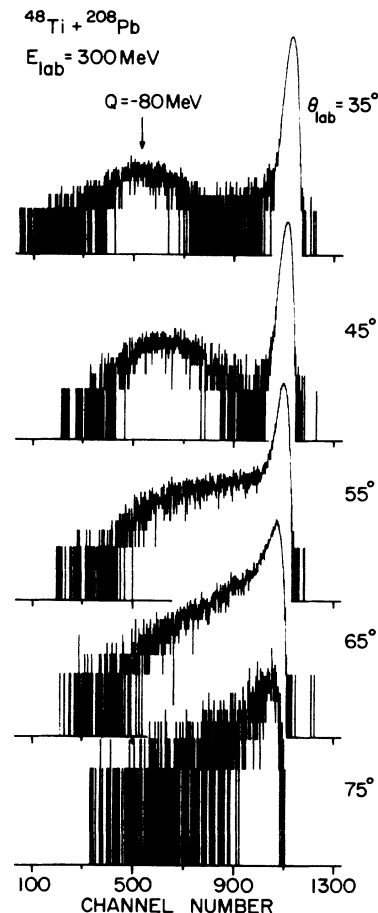


FIG. 4. Energy spectra from the reaction $^{48}\text{Ti} + ^{208}\text{Pb}$ at different scattering angles.

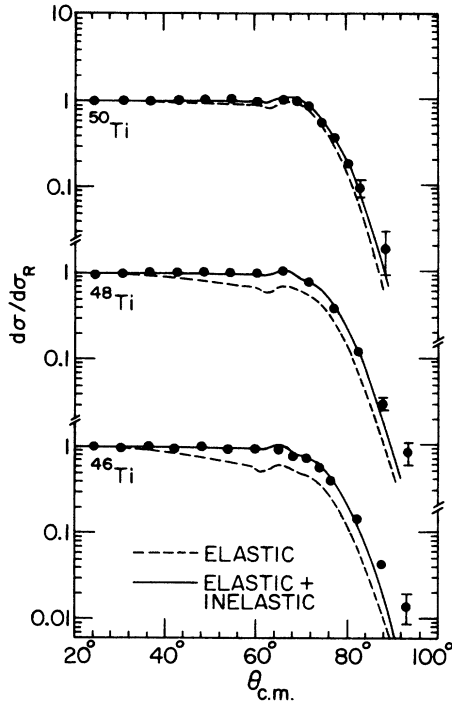


FIG. 5. Angular distributions for elastic scattering (including inelastic excitations up to 3 MeV) measured for the systems $^{46,48,50}\text{Ti} + ^{208}\text{Pb}$ at $E_{\text{lab}} = 298, 300, 302$ MeV, respectively. The lines are the result of coupled-channel calculations as explained in the text.

only slightly in the angular region $60^\circ \leq \theta_{\text{c.m.}} \leq 75^\circ$, with ^{46}Ti showing a small dip in $\sigma/\sigma_{\text{Rutherford}}$ near 68° as compared to ^{50}Ti . The solid and dashed lines are the result of coupled-channel calculation which will be described in more detail in Sec. IV A.

B. Transfer reactions

As can already be seen from the mass and Z spectra (Figs. 1 and 2), transfer reactions are dominated by the neutron-pickup reactions $^{208}\text{Pb}(^A\text{Ti}, ^{A+1}\text{Ti})^{207}\text{Pb}$. Angu-

lar distributions obtained from reactions induced by the three isotopes $^{46,48,50}\text{Ti}$ are shown in Fig. 6. They are generally bell shaped with a maximum around $\theta = 70^\circ$. The distributions for the neutron-pickup reactions ($^A\text{Ti}, ^{A+1}\text{Ti}$) and ($^A\text{Ti}, ^{A+2}\text{Ti}$) are identical within experimental uncertainty for the three isotopes. Large differences in the cross sections for neutron-exchange reactions ($^A\text{Ti}, ^{A-1}\text{Ti}$), with ^{46}Ti showing the lowest and ^{50}Ti the highest cross sections. The systematics of these cross sections will be discussed in detail in Sec. IV B.

Transfer reactions involving the exchange of charged particles (in particular stripping reactions) also show angular distributions peaked around the grazing angle. With increasing charge transfer, however, an additional forward-peaked component becomes more and more important. This is shown in Fig. 7 for several different elements observed in the reaction $^{48}\text{Ti} + ^{208}\text{Pb}$. These angular distributions are integrated over all excitation energies and over all isotopes with a given Z . The increasing importance of the forward-peaked component, especially for $Z \leq 20$ and for proton-pickup channels, is evident. The solid curves in Fig. 7 are least-squares fits to the data using a parametrization discussed in Sec. IV B. The reactions induced by ^{46}Ti and ^{50}Ti gave similar results.

With the higher-beam currents (and consequently better statistics) achieved for ^{48}Ti , angular distributions for individual isotopes could be investigated. In order to obtain a better understanding of the angular distributions, and in particular the origin of the two components mentioned above, Wilczyński plots¹³ (i.e., contour lines of constant cross section in a Q -value versus c.m.-angle plane) were deduced from these data. Figures 8 and 9 show these plots for different outgoing channels from the $^{48}\text{Ti} + ^{208}\text{Pb}$ system. As opposed to previous studies where the quasi-elastic region could not be separated from the large elastic component, our data allow a detailed study of the different reactions even for channels which are in the immediate vicinity of the projectile. Common to all Wilczyński plots shown in Figs. 8 and 9 is an orbiting component, i.e., a movement of the angular distribution towards smaller scattering angles with decreasing Q values. This movement can be quantitatively

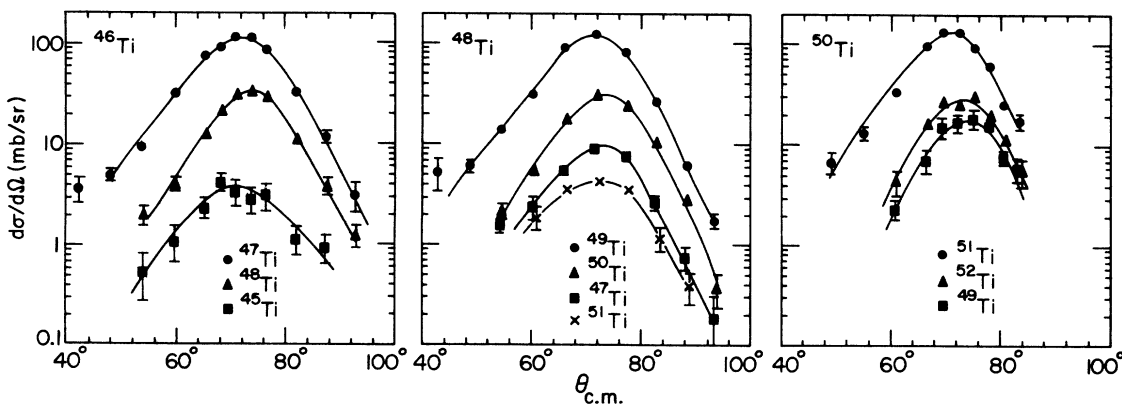


FIG. 6. Angular distributions for several neutron-transfer reactions induced by $^{46,48,50}\text{Ti}$ on ^{208}Pb . The solid lines serve to guide the eye.

described (see dashed line in Fig. 8) by macroscopic calculations which will be discussed in Sec. IV D. Superimposed on this orbiting component we find additional contributions which are especially pronounced for reaction products with $Z = 21, 22$. This component is correlated with small- Q values and peaks around the grazing angle ($\theta = 71^\circ$). For the neutron-pickup reactions ($^{48}\text{Ti}, ^{49}\text{Ti}$) and ($^{48}\text{Ti}, ^{50}\text{Ti}$) this component extends to very small angles. This effect, which is caused by the low binding energies of the exchanged particles (see Sec. IV C), results in two separated contributions to the energy spectrum in the $^{208}\text{Pb}(^{48}\text{Ti}, ^{49}\text{Ti})^{207}\text{Pb}$ reaction at forward angles, a quasi-elastic component correlated with small Q values, and a second contribution from the orbiting component showing much larger energy losses. For reaction products which are further away from the projectile ($Z = 22$,

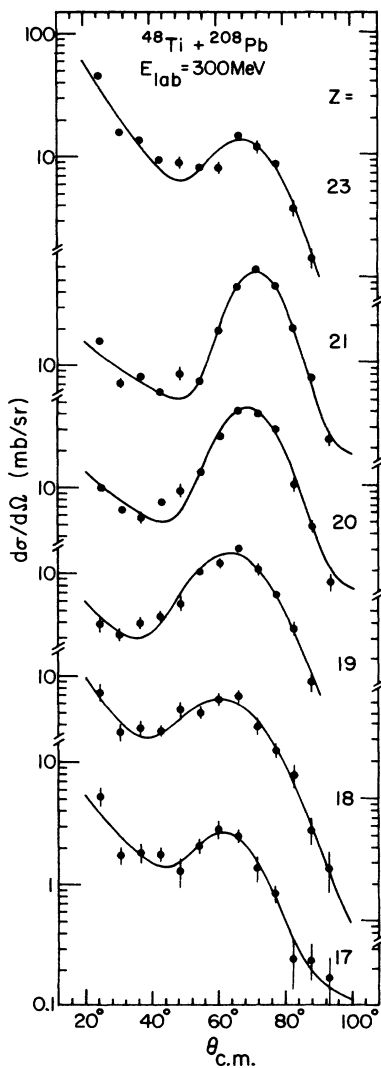


FIG. 7. Angular distributions for charge-transfer reactions (integrated over all isotopes and all excitation energies) for outgoing particles with $Z = 17-21$ and $Z = 23$ from the reaction $^{48}\text{Ti} + ^{208}\text{Pb}$. The solid lines are least-squares fits to the data, as described in the text.

$M = 48$), the quasi-elastic component is of lesser importance.

Since in this experiment only secondary mass and Z distributions have been measured, we have investigated to what extent subsequent particle evaporation influences the measured distributions. For that, evaporation calcu-

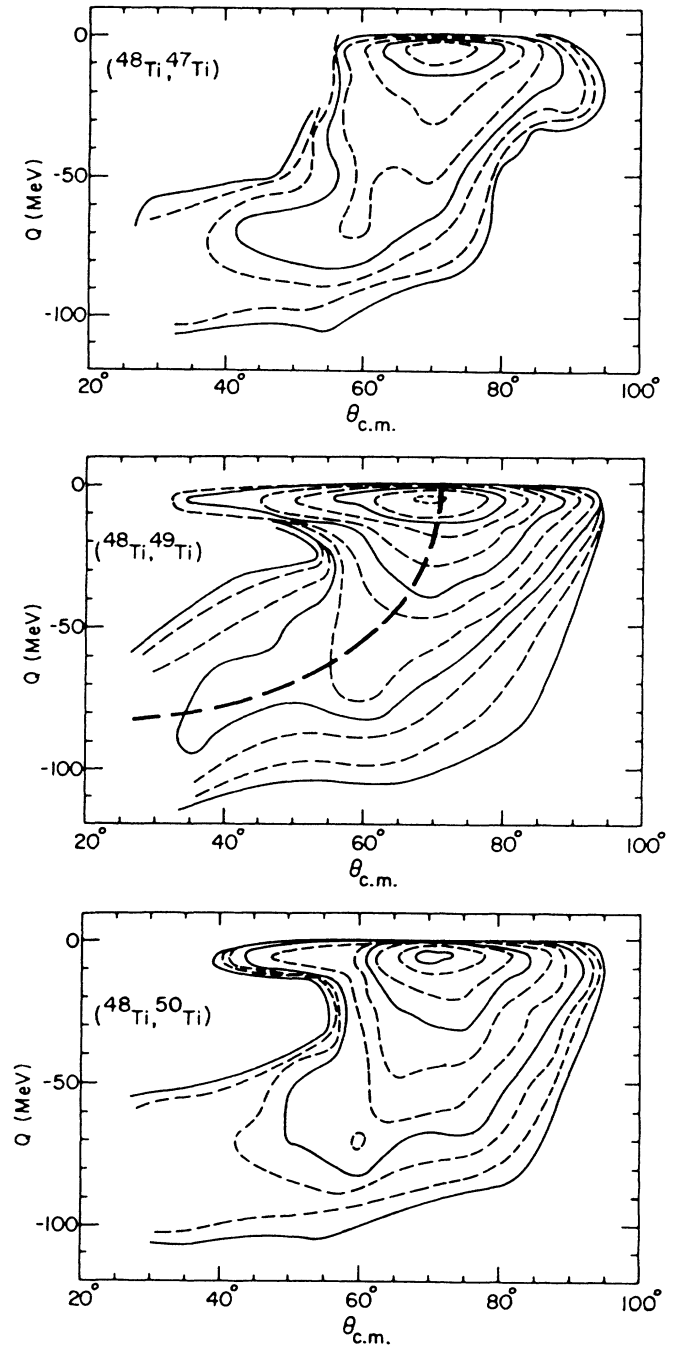


FIG. 8. Wilczyński plots for the reactions ($^{48}\text{Ti}, ^{47}\text{Ti}$), ($^{48}\text{Ti}, ^{49}\text{Ti}$), and ($^{48}\text{Ti}, ^{50}\text{Ti}$) on ^{208}Pb at $E_{\text{lab}} = 300$ MeV. The outermost solid contour line corresponds to a cross section of 0.01 mb/(rad MeV) with an increase by a factor of 10 for each subsequent line. The dashed lines correspond to cross sections of 2 or 5 times the values for the solid lines. The thick dashed line is the result of a macroscopic calculation as described in Sec. IV D.

lations with the code PACE (Ref. 18) were performed. Since no information is available for this system on how the excitation energy is distributed between the ejectile and the residual nucleus, energy sharing proportional to the mass of the two particles in the outgoing channel was assumed. From those calculations we find that the cross-section strengths for the Ti, Sc, and Ca isotopes are only weakly affected by evaporation effects, while for K isotopes the calculated primary mass distribution is peaked about one mass unit higher than measured experimentally. The shape of the Wilczyński plots for the orbiting component (similar for all channels investigated in this paper) are found to be unaffected by these evaporation effects. Considering the many assumptions going into these calculations and also noting that the evaporation effects are generally low at these bombarding ener-

gies, no evaporation corrections as used, e.g., in Ref. 19, were applied to the data.

C. Integrated cross sections

The integrated cross sections for the different reaction products resulting from $^{46,48,50}\text{Ti}$ incident on ^{208}Pb are shown in Fig. 10. Their sum is generally of the order of 1000–1100 mb. For the integration, the cross sections were extrapolated towards smaller and larger angles using the parametrization discussed in Sec. IV B. The cross section for $Z=22$ does not include inelastic-scattering contributions and hence represents the transfer strength only. While the neutron transfer cross section is quite independent of the projectile, the relative contributions for charge-pickup and charge-stripping reaction channels

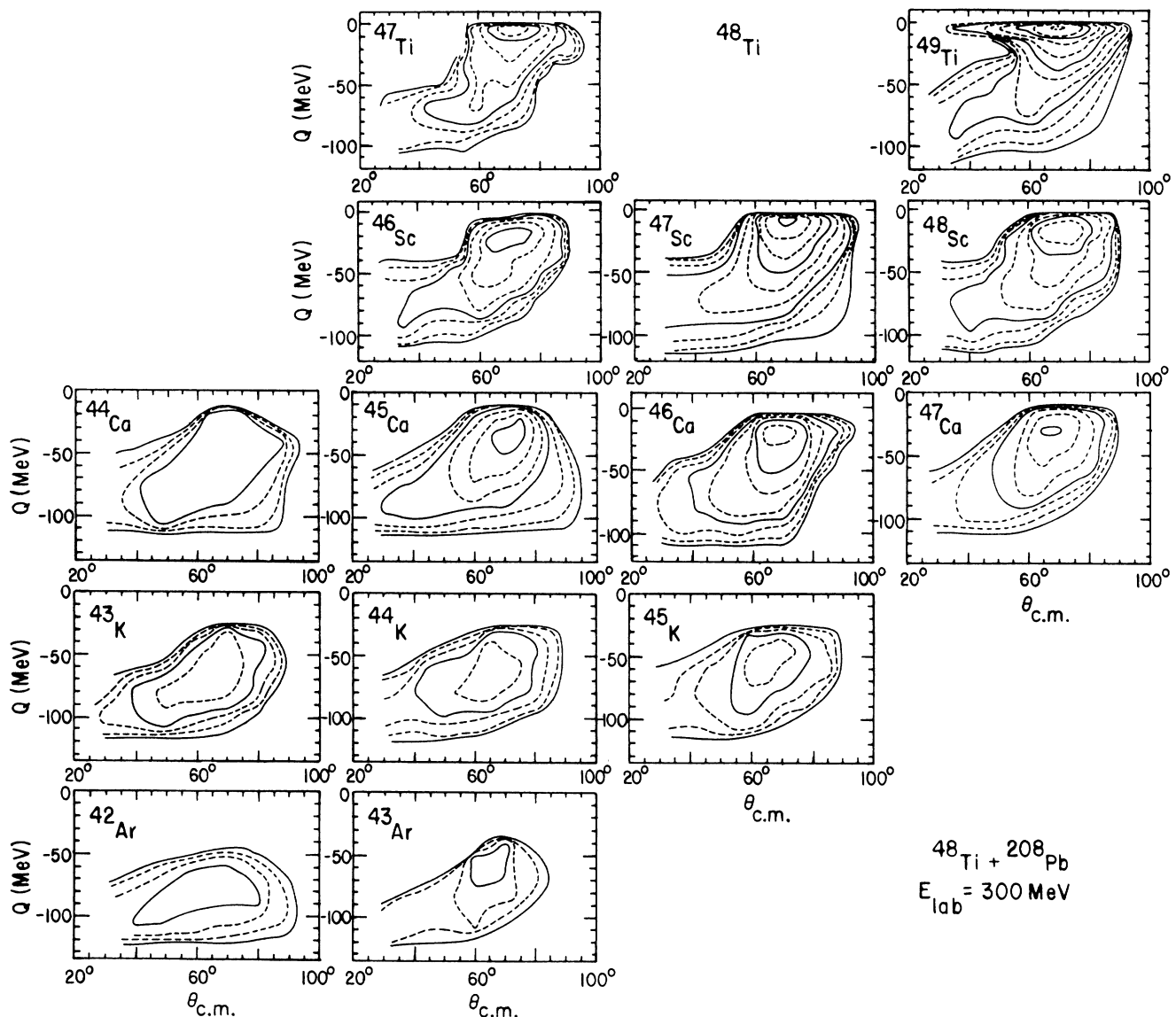


FIG. 9. Wilczyński plots for several transfer reaction channels induced by ^{48}Ti on ^{208}Pb at $E_{\text{lab}} = 300$ MeV. The values for the contour lines are the same as in Fig. 8.

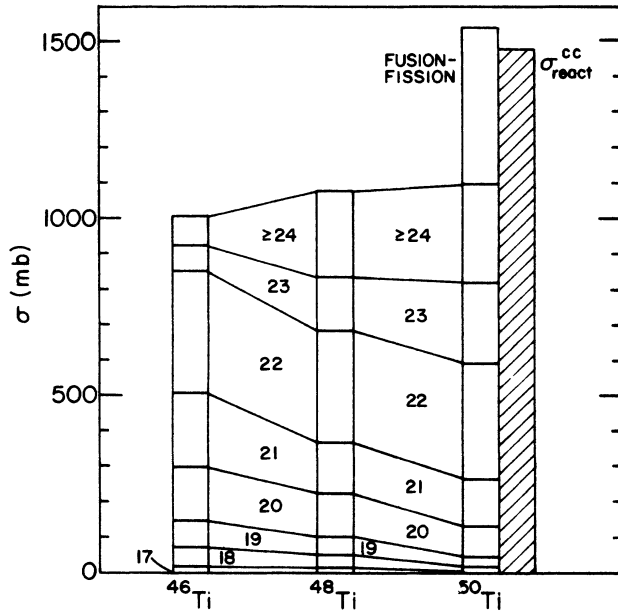


FIG. 10 Integrated cross section for different transfer reactions induced by $^{46,48,50}\text{Ti}$ on ^{208}Pb . Contributions for different particles are labeled with their respective Z . The cross section for the fusion-fission channel is taken from Ref. 20 and the coupled-channel reaction cross section is discussed in Sec. IV A.

changes in going from ^{46}Ti to ^{50}Ti . For ^{46}Ti induced reactions, outgoing particles with $Z \geq 23$ contribute only 15% of the total transfer cross section. This value increases to about 45% for the system $^{50}\text{Ti} + ^{208}\text{Pb}$. This behavior, which results from the Q -value differences for these reactions, will be discussed in Sec. IV B. With the better statistics in the case of ^{48}Ti , angular distributions for individual isotopes can be integrated. The results are shown in Fig. 11, which again illustrates the strong dominance of the neutron-pickup reaction $^{208}\text{Pb}(^{48}\text{Ti}, ^{49}\text{Ti})^{207}\text{Pb}$.

IV. DISCUSSION

A. Elastic and inelastic scattering

Because of the use of thick Pb targets, no separation of inelastic excitations from elastic scattering was possible in the present experiment. The angular distributions shown in Fig. 5 contain contributions from excited states up to an excitation energy of about 3 MeV. In this excitation energy region the main contributions are expected to come from the first excited 2^+ state in $^{46,48,50}\text{Ti}$ and the 3^- state in ^{208}Pb . We have not tried to determine optical-model parameters from a fit to the data, but rather used potential parameters which have already successfully described²¹ a somewhat lighter system ($^{58}\text{Ni} + ^{64}\text{Ni}$) at energies in the vicinity of the Coulomb barrier. The curves shown in Fig. 5 are the result of coupled-channel (CC) calculations with the program PTOLEMY,²² including coupling to the first 2^+ states in $^{46,48,50}\text{Ti}$ and to the 3^- state in ^{208}Pb . The $B(E2)$ values used were $0.09 e^2 b^2$, $0.072 e^2 b^2$, and $0.032 e^2 b^2$ for ^{46}Ti , ^{48}Ti , and ^{50}Ti , respec-

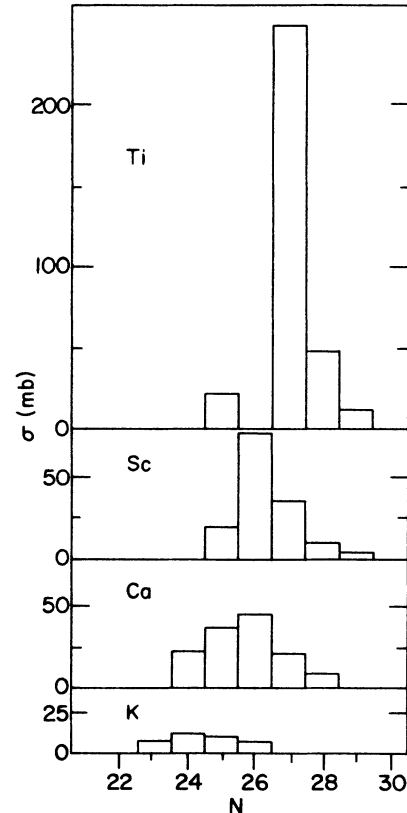


FIG. 11. Integrated cross section for individual isotopes with neutron number N produced in the collision of ^{48}Ti with ^{208}Pb at $E_{\text{lab}} = 300$ MeV.

tively (see Refs. 23–25) and $B(E3) = 0.665 e^2 b^3$ for ^{208}Pb (Ref. 26). Equal deformation lengths for charge and mass deformations were assumed. In the calculation the incident energy was corrected for the energy loss in the target. The dashed lines in Fig. 5 are the CC result for pure elastic scattering. For the solid lines, the contributions from the two inelastic channels have been added to the elastic scattering cross section. Since ^{46}Ti has the highest $B(E2)$ value of all three Ti isotopes, the difference between the solid and dashed curve is largest for the lightest Ti isotope. The agreement between the solid line and the data is generally quite good, particularly since no change to the potential parameters of Ref. 21 has been made. The disagreement seen at large angles for the $^{46}\text{Ti} + ^{208}\text{Pb}$ system might result from neglecting higher excited 2^+ and 4^+ states in the CC calculations for ^{46}Ti .

TABLE I. Integrated cross sections (in mb) obtained from the coupled-channel calculations.

	^{46}Ti	^{48}Ti	^{50}Ti
σ_{react}	3910	3400	2140
$\sigma_{2^+}(\text{Ti})$	2520	1940	590
$\sigma_{3^-}(\text{Pb})$	80	80	80
$\sigma_{\text{inelastic}}$	2600	2020	670
σ_{reduced}	1310	1380	1470
$\sigma_{1/4}$	1460	1460	1460

The integrated cross sections from these calculations for the three systems are summarized in Table I. As can be seen, there is a strong decrease in the inelastic-scattering yield in going from ^{46}Ti to the closed-neutron-shell nucleus ^{50}Ti . This decrease, which is about a factor of 4, seems however to have no significant effect on the transfer cross sections to be discussed in the following sections. The fifth line in Table I gives the “reduced reaction cross section,” defined as the total reaction cross section reduced by the inelastic-scattering contributions. This “reduced cross section” is available for fusion-fission processes and for transfer reactions. A comparison of this “reduced cross section” with the result of the modified quarter-point recipe²⁷

$$\sigma_r = \frac{\pi\Lambda^2}{k^2} \left[1 + \frac{2\Delta}{\Lambda} \right], \quad (1)$$

where k is the wave number, Λ the critical angular momentum (deduced from the quarter-point angle), and Δ the diffuseness of the l distribution (taken from optical-model calculations to be $\Delta=7$) shows that both values are in quite good agreement, in particular for $^{50}\text{Ti}+^{208}\text{Pb}$ where the agreement between data and the theoretical calculations using this *ad hoc* potential is best.

B. Cross-section systematics: quasi-elastic and deep-inelastic reactions

As can be seen from the Wilczyński plots (Fig. 9), no clear separation exists between the forward-peaked orbiting component and the Gaussian component centered around the grazing angle. Deep-inelastic processes seem to evolve gradually from the quasi-elastic reactions. This is contrary to what has been proposed by the authors of Ref. 28. However, in order to obtain some estimates of the cross sections associated with these two processes, two methods for separating the components have been attempted. One method involves an (arbitrary) energy cut at $Q = -30$ MeV in the energy spectra. This choice arises from the observation that at this Q value a minimum in the energy spectra at forward angles is observed (see Fig. 4). Associating all events with $Q > -30$ MeV with quasi-elastic reactions, and the ones with $Q < -30$ MeV with deep-inelastic processes, we obtain for $^{46,48,50}\text{Ti}$ the results given in the first two columns of Table II. The second method of distinguishing the two reaction components involves a parameterization of the angular distributions using the expression

$$\frac{d\sigma}{d\theta} = A \exp(-\lambda\theta) + B \exp[-(\theta - \bar{\theta})^2 / (2\sigma^2)]. \quad (2)$$

TABLE II. Cross sections (in mb) for quasi-elastic and deep-inelastic processes measured for the systems $^{46,48,50}\text{Ti}+^{208}\text{Pb}$. The methods to distinguish between the two processes are described in the text.

	σ_{QE}	σ_{DI}	σ_G^E	σ_{exp}^{DI}	σ_{trans}
^{46}Ti	500	510	590	420	1010
^{48}Ti	450	620	550	520	1070
^{50}Ti	480	620	490	610	1100

This angle dependence is similar to that used by Mikumo *et al.*²⁹ and later by Brosa and Westmeier.²⁸ The coefficients A , B , λ , $\bar{\theta}$, and σ^2 were determined from least-squares fits to the data. Examples of this parameterization are shown as solid lines in Fig. 7. If we associate the forward-peaking exponential component of Eq. (2) with deep-inelastic scattering, and the Gaussian component with quasi-elastic processes, we obtain integrated cross sections as shown in columns 3 and 4 of Table II. The cross sections for all transfer processes are given in the last column.

The total transfer cross section for all three Ti isotopes $\sigma_{\text{transfer}} = 1050$ mb is consistent within about $\pm 5\%$. Adding the contribution for fusion-fission reactions²⁰ measured for the system $^{50}\text{Ti}+^{208}\text{Pb}$ ($\sigma_{ff} = 440$ mb) to the transfer cross section, we obtain $\sigma_{\text{react}} = 1540$ mb, in very good agreement with the result obtained from the coupled-channel calculation or from the simple quarter-point recipe. We further observe from Table II that the cross section associated with quasi-elastic transfer reactions is about 50% of the total transfer cross section, independent of the method chosen to separate the two processes. There is an increase of the exponential component of the angular distributions in going from ^{46}Ti to ^{50}Ti which suggests a larger fraction of “deep-inelastic” reactions for the more neutron-rich projectile. Similar effects have been observed for the system $^{58,64}\text{Ni}+^{208}\text{Pb}$ (Ref. 30). With the uncertainties in the separation techniques, however, no definite conclusion can be drawn from the present data as to whether neutron-rich projectiles actually favor deep-inelastic reactions.

The individual contributions from the exponential and the Gaussian components of the angular distributions for the production of different elements in the $^{46,48,50}\text{Ti}+^{208}\text{Pb}$ reactions are shown in Fig. 12. The quasi-elastic contributions are strongly dominated by neutron-transfer processes and charge-stripping reactions (Ti,Sc), (Ti,Ca), while the probability for a quasi-elastic charge-pickup reaction (Ti,V) is very small. This behavior is also observed in transfer reactions induced by lighter projectiles (e.g., $^{16}\text{O}+^{208}\text{Pb}$), where it is explained as resulting from Q -matching considerations^{31,32} which strongly favor the reaction ($^{16}\text{O},^{15}\text{N}$) as compared to ($^{16}\text{O},^{17}\text{F}$).

Two more quantities can be extracted from the shape of the angular distributions. As can be seen from Fig. 7, there is a continuous shift of the Gaussian, quasi-elastic part of the angular distribution towards forward angles as more charge is transferred between projectile and target. Figure 13 shows the values for the centroids $\bar{\theta}$ and the variances σ^2 [defined in Eq. (2)] as a function of the charge Z of the outgoing particles, obtained from least-squares fits to the angular distributions for $^{48}\text{Ti}+^{208}\text{Pb}$. With decreasing Z , the centroid angle of the quasi-elastic part of the angular distribution first increases (in going from $Z = 23$ to $Z = 21$) and then moves to smaller values. At the same time, the variance of the distribution increases by about a factor of 3. Some of this behavior is caused by the change in energy and charge of the outgoing particles during the interaction and can be simply understood within semiclassical models. The solid line in

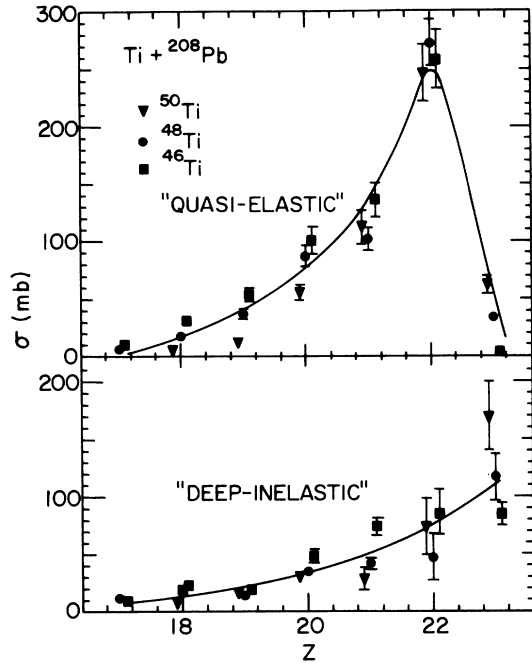


FIG. 12. Cross sections as obtained from the Gaussian (top) and exponential (bottom) component in the angular distribution for production of different reaction products with charge number Z in the reactions $^{46,48,50}\text{Ti} + ^{208}\text{Pb}$. The lines serve to guide the eye.

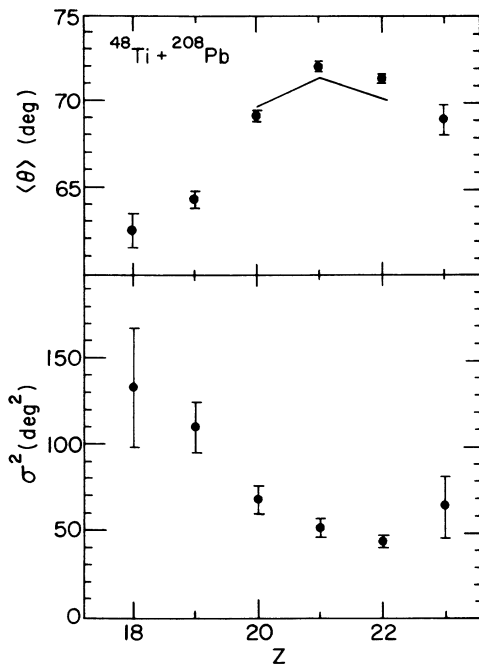


FIG. 13. Centroids and variances of the Gaussian part of the angular distributions (see Fig. 7) as function of the charge Z of the outgoing particles for the system $^{48}\text{Ti} + ^{208}\text{Pb}$. The solid line connects the DWBA prediction for one- and two-particle-transfer reactions as explained in the text.

Fig. 13 is the result of DWBA calculations for one- and two-nucleon transfer reactions [$(^{48}\text{Ti}, ^{49}\text{Ti})$, $(^{48}\text{Ti}, ^{47}\text{Sc})$, and $(^{48}\text{Ti}, ^{46}\text{Ca})$] using the same potential as discussed in Sec. IV A. The trend for the centroids of the angular distributions, which are bell shaped, are quite well reproduced for these reactions. Within macroscopic models,³³ the forward shift of the angular distributions is interpreted as resulting from a rotation of the dinuclear complex. From the slope in Fig. 13, we can deduce a rotation angle of about 3.5° for the transfer of one charge from projectile to target. If in a simple semiclassical model we assume that these processes occur at an angular momentum of $l = 125\hbar$, which is slightly smaller than the critical l value deduced from the quarter-point angle, we can calculate from this rotation angle the interaction time necessary to exchange one proton. For a collision with a moment of inertia calculated under the nonsticking assumption³ ($r_0 = 1.45$ fm), a transfer time of 5.8×10^{-23} sec is obtained.

Since cross sections for all reaction processes (fusion-fission,²⁰ quasi- and deep-inelastic transfers) have been measured for the system $^{50}\text{Ti} + ^{208}\text{Pb}$, critical angular momenta for the different reactions can be calculated within a sharp-cutoff model. The results are shown in Fig. 14. Also shown is the calculated inelastic-scattering contribution (see Sec. IV A). This is the first time a complete partition of σ_{react} has been obtained for such a heavy system. It is clear from Fig. 14 that quasi-elastic processes in reactions between heavy ions are substantial. Rather than being a negligible component of the total reaction cross section as has been assumed in several previous publications,^{34,35} the quasi-elastic component is of the same order of magnitude as the fusion-fission and deep-inelastic processes.

C. Neutron transfer reactions

The investigation of $^{46,48,50}\text{Ti}$ -induced transfer reactions allows a detailed study of the influence of nuclear structure effects on the strong neutron-transfer reactions, which have been measured in several sys-

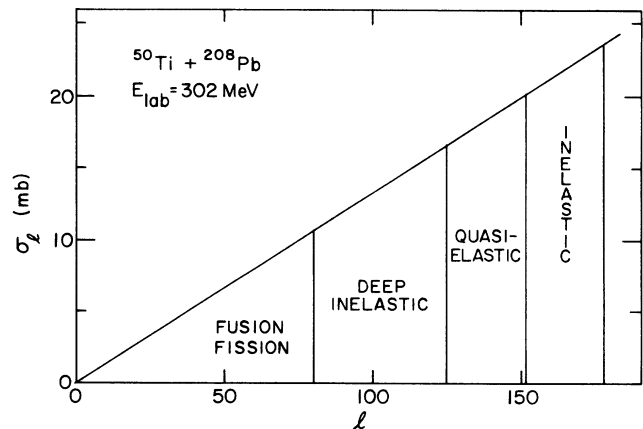


FIG. 14. Contributions of the different reaction processes to the total reaction cross section for the system $^{50}\text{Ti} + ^{208}\text{Pb}$ at $E_{\text{lab}} = 302$ MeV, assuming a sharp-cutoff model.

tems.^{5,6,10-12,36,37} The ground-state Q values for different neutron-transfer reactions are summarized in Table III. They differ by as much as 6 MeV for ^{46}Ti and ^{50}Ti induced reactions. Also, as already discussed in Sec. IV A, there is a large difference in the strength of the inelastic excitation between ^{46}Ti and ^{50}Ti which could also influence the neutron-transfer channel. Furthermore, due to the closed neutron shell at $N=28$, the spectroscopic factors for the single-particle levels involved in neutron-transfer reactions change considerably in going from ($^{46}\text{Ti}, ^{47}\text{Ti}$) to ($^{50}\text{Ti}, ^{51}\text{Ti}$). Considering these many differences between the three Ti isotopes, it is remarkable that the cross sections for the one-neutron-pickup reaction $^{208}\text{Pb} (^A\text{Ti}, ^{A+1}\text{Ti}) ^{207}\text{Pb}$ are the same within the experimental uncertainties for the three Ti isotopes. This is also true for the two-neutron-pickup reactions $^{208}\text{Pb} (^A\text{Ti}, ^{A+2}\text{Ti}) ^{206}\text{Pb}$, while the cross sections for the neutron-stripping reactions $^{208}\text{Pb} (^A\text{Ti}, ^{A-1}\text{Ti}) ^{208}\text{Pb}$ increase by almost a factor of 4 in going from ^{46}Ti to ^{50}Ti . It should be noted that the cross sections for neutron-transfer reactions do not follow the Q_{gg} systematics,³⁸ which would predict the largest cross sections for the two-neutron-transfer reaction.

In order to see to what extent simple one-step DWBA calculations are able to describe the cross sections, we have performed PTOLEMY (Ref. 22) computations with the same scattering potential used for the coupled-channel calculations mentioned in Sec. IV A. The bound-state parameters used were $r_0=1.20$ fm and $a=0.65$ fm. The $\frac{3}{2}^-$, $\frac{1}{2}^-$, $\frac{5}{2}^-$, $\frac{7}{2}^-$, and $\frac{9}{2}^+$ states of the projectile, and the $\frac{1}{2}^-$, $\frac{3}{2}^-$, $\frac{5}{2}^-$, $\frac{7}{2}^-$, $\frac{9}{2}^-$, and $\frac{13}{2}^+$ states of ^{207}Pb were included in the calculations. The spectroscopic factors were taken from (d,p) or (p,d) reactions (see Table IV). To reduce the number of calculations, the fragmented $\frac{3}{2}^-$, $\frac{1}{2}^-$, and $\frac{7}{2}^-$ strength in the Ti isotopes was assumed to be concentrated in a single state centered at the center of gravity of the different states shown in Table IV. This procedure resulted in cross sections which differed by only a few percent from a full calculation. Considerably larger uncertainties are associated with the spectroscopic factors which are usually accurate only to about 20%. Figure 15 shows the comparison of the data ($|Q| \leq 10$ MeV) with the calculated angular distribution. The calculated distribution results from summing individual distributions obtained for the states quoted in Table IV. The peak location and height of the angular distribution is well reproduced, whereas the width is underpredicted by about 60%. The integrated theoretical cross section is 106 mb as compared to the experimental cross section of 180 mb. Such a comparison has to take into account, however, that only states at low

excitation energies ($E^* < 7$ MeV) are included in the DWBA calculation. States at higher excitation energies are probably populated via more complicated multistep processes which were not included in the simple one-step DWBA calculation.

Similar calculations performed for the reactions $^{208}\text{Pb} (^{46}\text{Ti}, ^{47}\text{Ti}) ^{207}\text{Pb}$ and $^{208}\text{Pb} (^{50}\text{Ti}, ^{51}\text{Ti}) ^{207}\text{Pb}$ with the appropriate spectroscopic factors gave integrated cross sections of 106 and 109 mb, respectively. This indicates that the differences in spectroscopic strength are diminished when the sum of many states is calculated in a nuclear-transfer reaction.

A simpler method to obtain values for the integrated one-neutron-transfer cross sections based on the kinematic matching conditions has been published recently.⁴¹ The data from $^{46,48,60}\text{Ti} + ^{208}\text{Pb}$ (which were included in these systematics) are very well described by this parametrization.

As already stated in Ref. 5, the quasi-elastic neutron-transfer reactions contribute an appreciable fraction to the total reaction cross sections. From the Wilczyński plots, it is furthermore observed that these processes occur already at small scattering angles which, in a semiclassical picture, correspond to large separations. A scattering angle of 40° corresponds in the system $^{48}\text{Ti} + ^{208}\text{Pb}$ to a distance of closest approach of about 20 fm, whereas the sum of the half-density radii of the two nuclei is about 12 fm. This emphasizes that neutron transfer takes place at a very early stage in the reaction, when the overlap of the two nuclei is very small and the wave functions of the transferred nuclei can be described by their asymptotic behavior.

It is well known from previous studies^{7,42,43} that the transfer cross section $d\sigma/d\Omega$ if plotted versus the distance of closest approach D shows an exponential falloff which is proportional to the square root of the binding energy E_B of the transferred particle:

$$\frac{d\sigma}{d\Omega} \sim \exp(-2\sqrt{2\mu_N E_B} \cdot D), \quad (3)$$

where μ_N is the reduced mass of the transferred particle. In Fig. 16 we have plotted the transfer probability P_t defined by

$$\left[\frac{d\sigma}{d\Omega} \right]_{\text{transfer}} = P_t \left[\frac{d\sigma}{d\Omega} \right]_{\text{elastic+inelastic}} \quad (4)$$

as function of the distance of closest approach, assuming that the particle moves on a pure Coulomb trajectory. The values for

$$(d\sigma/d\Omega)_{\text{elastic+inelastic}}$$

TABLE III. Ground-state Q values and integrated quasi-elastic cross sections for several neutron-transfer reactions induced by $^{46,48,50}\text{Ti}$ on ^{208}Pb . Q values in MeV, σ in mb.

	$(^A\text{Ti}, ^{A-1}\text{Ti})$		$(^A\text{Ti}, ^{A+1}\text{Ti})$		$(^A\text{Ti}, ^{A+2}\text{Ti})$	
	Q	σ	Q	σ	Q	σ
^{46}Ti	-9.259	7±2	1.506	210±20	6.394	56±6
^{48}Ti	-7.69	17±3	0.775	225±20	4.982	54±5
^{50}Ti	-7.010	28±3	-0.992	205±20	0.070	45±5

TABLE IV. Single-particle states and spectroscopic factors used in the DWBA calculation for the reaction $^{208}\text{Pb}(^{48}\text{Ti}, ^{49}\text{Ti})^{207}\text{Pb}$. The values for ^{207}Pb were taken from the ($^{16}\text{O}, ^{17}\text{O}$) results in Ref. 39, and those for ^{49}Ti from Ref. 40.

^{207}Pb			^{49}Ti		
State	E^* (MeV)	$(2j+1)S$	State	E^* (MeV)	$(2j+1)S$
$3p_{1/2}$	0	1.90	$2p_{1/2}$	1.724	0.65
$3p_{3/2}$	0.89	4.28		3.176	0.34
$2f_{5/2}$	0.57	4.80		4.222	0.13
$2f_{7/2}$	2.34	6.40		4.667	0.19
$1h_{9/2}$	3.47	7.50	$2p_{3/2}$	1.385	2.47
$1i_{13/2}$	1.63	4.76		1.587	0.06
				3.261	0.73
			$1f_{7/2}$	0.0	1.89
				2.472	0.45
			$1g_{9/2}$	4.770	3.16

were taken from Fig. 5. The solid line corresponds to an exponential decay curve [see Eq. (3)] with $E_b = 7.376$ MeV, i.e., the binding energy of a neutron in ^{208}Pb .

It can be seen from Fig. 16 that even at distances of $D = 20$ fm, transfer probabilities of several times 10^{-4} are observed. The transfer probability for large distances is quite well described by the exponential behavior given in Eq. (3). At $D = 14$ fm, a kink in the transfer probability is observed just as in Ref. 42. At these distances, other transfer processes start to dominate and the applicability of Eq. (4) becomes questionable.

D. Deep-inelastic reactions

As can be clearly seen from Figs. 4, 8, and 9, we observe in the reaction $^{48}\text{Ti} + ^{208}\text{Pb}$, especially at forward angles, a well-developed deep-inelastic component which is associated with an average energy loss of about 80 MeV. Taking into account that the incident energy is only about 45 MeV above the Coulomb barrier of the entrance channel, strongly deformed configurations must have been formed in these collisions. The cross section

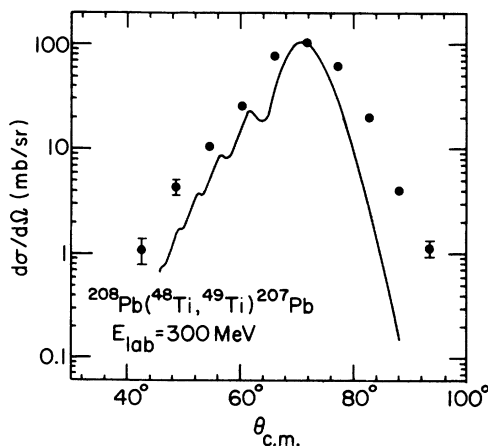


FIG. 15. Angular distribution measured for the reaction $^{208}\text{Pb}(^{48}\text{Ti}, ^{49}\text{Ti})^{207}\text{Pb}$ at $E_{\text{lab}} = 300$ MeV. Only events with a Q value larger than -10 MeV are included. The solid line is the result of a DWBA calculation as discussed in the text.

associated with these deep-inelastic reactions is about $\frac{1}{3}$ of the total reaction cross section (see Table II) and, as can be seen from the Wilczyński plots (Figs. 8 and 9), all reaction channels show this orbiting component.

Several models have been developed in order to understand the deep-inelastic process.⁴⁴ They are primarily based on the stochastic exchange of particles between the two reaction partners and are thus applicable mainly to the later stages of a collision, when the number of particle exchanges is large enough to justify a statistical treatment. The main quantities which have been compared with experimental data are the first and second moments of the mass, charge, energy, and angular momentum distributions. In general, the agreement is quite good. Here we shall only discuss briefly model descriptions of these average quantities and concentrate instead on our new results which show the transition between quasi-elastic and deep-inelastic processes (see Sec. IV E).

Figure 17 shows the first (centroid) and second (variance) moments of the mass and charge distributions obtained from the $^{48}\text{Ti} + ^{208}\text{Pb}$ spectra integrated over the angular range $\theta_{\text{lab}} = 20^\circ - 80^\circ$, as a function of the Q value. It should be pointed out that these are secondary distributions and no correction for particle evaporation

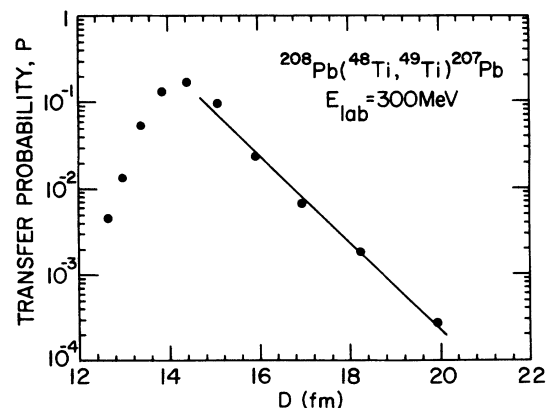


FIG. 16. Transfer probability $P_i = d\sigma/d\Omega / (d\sigma/d\Omega)_{\text{elastic}}$ for the reaction $^{208}\text{Pb}(^{48}\text{Ti}, ^{49}\text{Ti})^{207}\text{Pb}$ plotted vs the distance of closest approach D . The solid line is explained in the text.

has been made. As shown by several authors^{8,45,47} such corrections mainly influence the first moment of the mass distributions, particularly for Q values less than -50 MeV, whereas the effect on the mass and charge variance is small. Evaporation calculations with the code PACE,¹⁸ already mentioned in Sec. III B, confirm these observations for our systems.

The centroid of the mass distribution for small energy losses is larger than the incident mass of $A=48$. This effect is caused by the dominance of the quasi-elastic neutron-pickup reactions leading to ^{49}Ti . For more negative values of Q ($-Q \approx 25$ MeV) the centroid moves to $A \approx 47$ and remains at this value, up to $Q = -90$ MeV. Evaporation corrections at these Q values shift the centroids to larger-mass values by about one unit.

The centroid of the charge distribution starts at around $Z=22$ and moves to about $Z=21$ for $Q = -30$ MeV. The variances σ_A^2 and σ_Z^2 show a continuous increase with decreasing Q . It should be emphasized that the variances are obtained from spectra integrated in the angular range 20 – 80° . If only data near the grazing angle are included, σ_A^2 and σ_Z^2 decrease by about 30%. The dashed lines are derived from macroscopic-model calculations using the program of Feldmeier.³³ This model,

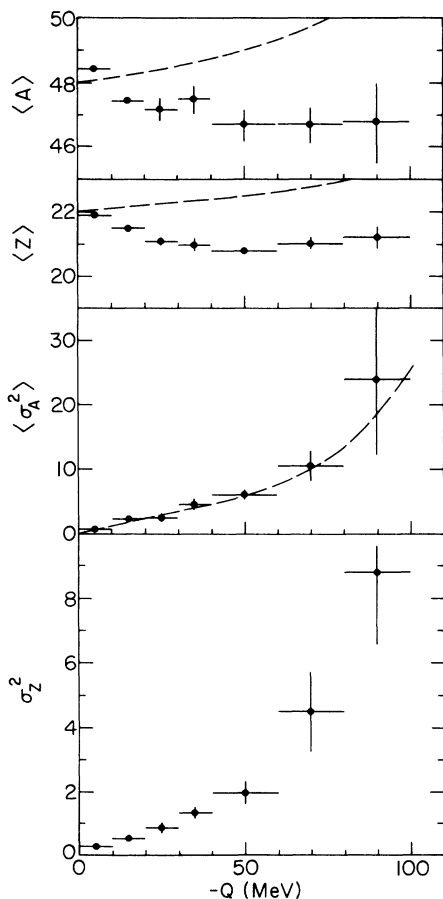


FIG. 17. First and second moments of the mass and charge distributions obtained in the reaction $^{48}\text{Ti} + ^{208}\text{Pb}$. The dashed lines are the result of a macroscopic calculation, as explained in the text.

which contains no adjustable parameters, describes the orbiting deep-inelastic component in the Wilczyński plots quite well (see Fig. 8). The same is true for the Q -value dependence of the mass variances σ_A^2 . The program fails, however, to correctly describe the shift of the centroids $\langle A \rangle$ and $\langle Z \rangle$ of the distributions towards smaller values in particular for small- Q values. This discrepancy mainly results from not treating neutrons and protons as independent particles and thus the equilibration of the N/Z degree of freedom in the early reaction stages can not be properly described. For the same reason, no prediction for σ_Z^2 can be made within this model.

The shift of $\langle Z \rangle$ and $\langle A \rangle$ towards larger asymmetry values has been observed in a variety of systems.^{4,8,11} In our case it is not easily explained as a consequence of the underlying driving potential. This potential is defined as the difference of the energies in the final and the initial channel

$$V_D = -Q_{gg} + V_f^{\text{Coul}} - V_i^{\text{Coul}} + V_f^{\text{rot}} - V_i^{\text{rot}} + V_f^{\text{nucl}} - V_i^{\text{nucl}}, \quad (5)$$

where Q_{gg} is the ground-state Q value for the particular reaction channel and $V_{i,(f)}^{\text{Coul}}$, $V_{i,(f)}^{\text{rot}}$, and $V_{i,(f)}^{\text{nucl}}$ are the Coulomb, rotational, and nuclear potential in the entrance (exit) channel, respectively. Figure 18 shows as an example the driving potential for the $^{48}\text{Ti} + ^{208}\text{Pb}$ system as calculated from Eq. (5). For Q_{gg} , measured mass excesses or predictions from the Garvey-Kelson mass formula were used.⁴⁸ For the Coulomb and centrifugal potential ($l=130\hbar$), homogeneous mass and charge distributions with a radius parameter $r_0=1.25$ fm were assumed. Since no information about ΔV^{nucl} is available, the contributions from the nuclear potential to Eq. (5) were neglected. The odd-even staggering in V_D and the minimum around the doubly-closed-shell nucleus ^{48}Ca can be seen from this figure. If we assume that the structure of the driving potential is the dominating factor determining the direction of the mass and charge flow, we expect from Fig. 18 a preferential formation of the neutron-rich isotopes of Ti (^{52}Ti), Sc (^{51}Sc), and Ca (^{48}Ca)

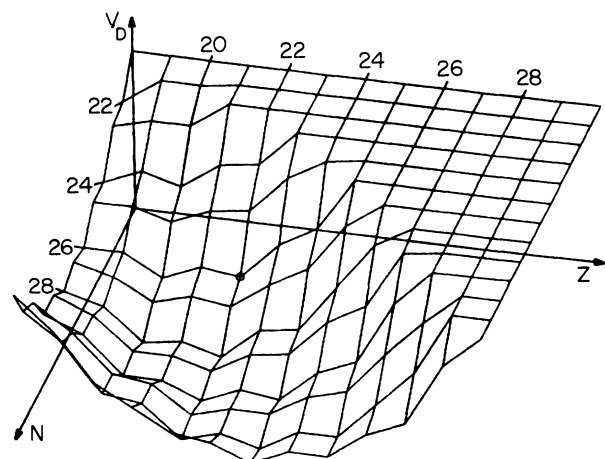


FIG. 18. Driving potential as calculated from Eq. (5) for the system $^{48}\text{Ti} + ^{208}\text{Pb}$.

with neutron numbers between 28–30. While the centroids of measured charge distributions (see Fig. 17) show a shift towards $Z = 21$ (Sc) in agreement with this expectation, the preferred production of neutron-rich nuclei is only observed for very small energy losses [dominated by the (^{48}Ti , ^{49}Ti) reaction], while for larger energy losses the centroid of the mass distributions stays at $\langle A \rangle = 47$, corresponding to a neutron number of $\langle N \rangle = 26$. It should be noted, however, that many of the assumptions made in the calculation of the driving potential (e.g., neglect of the nuclear contributions) are questionable for collisions that lead to a large overlap of the two interacting nuclei. Furthermore, effects of the nucleonic kinetic energy (“kinetic pressure”) in the two nuclei should not be neglected.⁴⁹

In the following, we shall investigate the entrance stage of the reaction, focusing on the Q -value spectra for several of the reaction products produced in the collision of $^{48}\text{Ti} + ^{208}\text{Pb}$.

E. The transition from quasi-elastic to deep-inelastic collisions

As discussed, we observe from the Wilczyński plots that the few nucleon-transfer reactions [e.g., (^{48}Ti , ^{49}Ti)] show a strong quasi-elastic component, centered around the grazing angle ($\theta_{\text{grazing}} = 70^\circ$), while more complicated transfers [e.g., (^{48}Ti , ^{43}K)] are dominated by an orbiting deep-inelastic component. This is further emphasized by projecting the Wilczyński plots onto the Q axis, as shown in Fig. 19 for several reaction channels. The Q -value spectra have been fitted by the sum of two Gaussian distributions whose parameters have been adjusted to the experimental data (see solid lines in Fig. 19).

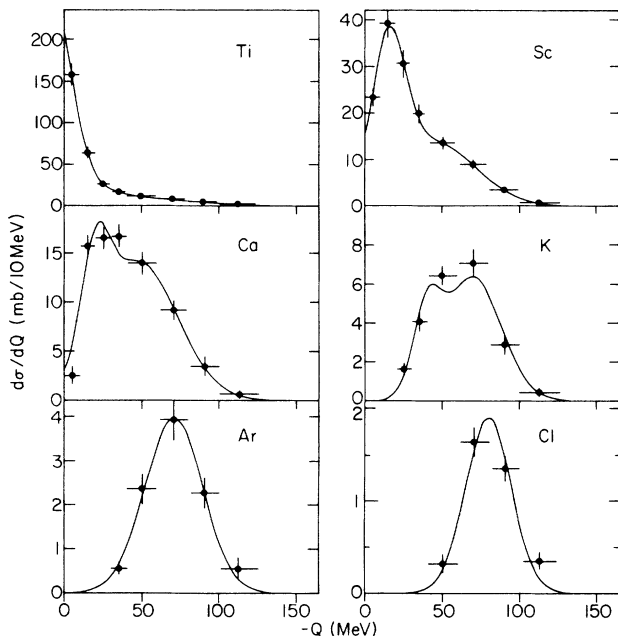


FIG. 19. Q -value spectra for several reaction channels for the reaction $^{48}\text{Ti} + ^{208}\text{Pb}$ as obtained from the projections of the corresponding Wilczyński plots onto the Q axis.

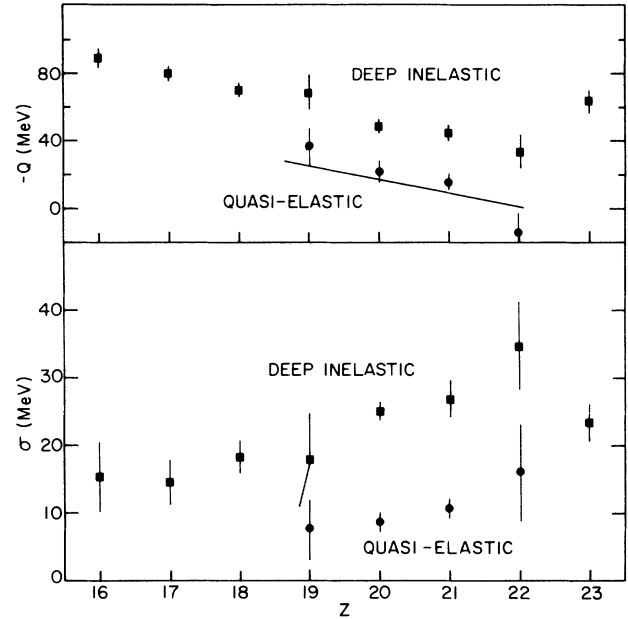


FIG. 20. Centroids of the two Gaussian distributions as obtained from least-squares fits to the Q -value spectra for reaction products with different charge Z . The solid line is a prediction using Q matching conditions as explained in the text.

The values for the centroids and the variances of the two Gaussian distributions are shown in Fig. 20 as function of the charge of the outgoing particle. The quasi-elastic component can be observed for reaction products with $Z = 19$ – 22 , whereas the second deep-inelastic component is present in all Q -value spectra. The Q -value centroids for both components decrease by about 9 MeV per transferred charge. The solid line in Fig. 20 is the prediction of the simple Q -matching model of Buttle and Goldfarb⁵⁰

$$Q = E_{\text{c.m.}}^{(i)} \left[\frac{Z'z'}{Zz} - 1 \right], \quad (6)$$

where $E_{\text{c.m.}}^{(i)}$ is the c.m. energy in the incoming channel and Zz and $Z'z'$ are the product of the charges in the entrance and exit channel, respectively. For one- and two-

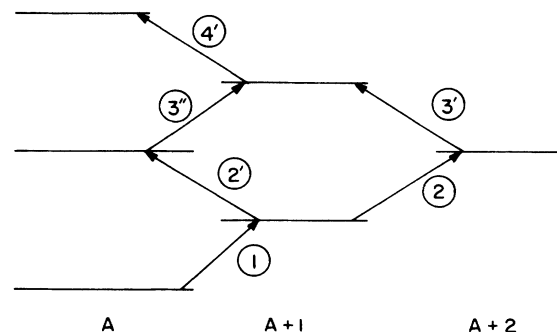


FIG. 21. Population of multiparticle-multihole states in reactions between heavy ions.

proton-transfer reactions, Eq. (6) is in very good agreement with DWBA calculations. The variances of the distributions are largest for reaction products with $Z=22$ and decrease for transfer reactions leading away from the entrance channel.

The nature of these two contributions and the behavior of the centroids can be understood within a simple model which is based on the population of particle-hole states in multistep collisions. The underlying principle is schematically illustrated in Fig. 21. Starting from a nucleus A (e.g., ^{208}Pb) we can populate states in the daughter nucleus $A+1$ (e.g., ^{209}Bi) in a one-step process. Due to the Q values involved, this interaction populates mainly one-particle states at low excitation energy. If the interaction time is long enough, a second transfer reaction can occur (step 2), leading to the nucleus $A+2$ where again two-particle states are populated. There is, however, also the possibility to go back to the nucleus A (step 2'), populating one-particle one-hole states. It is known from ($d, ^3\text{He}$) reactions on ^{209}Bi that these states, which lie around $E_x=5$ MeV in ^{208}Pb , are very strongly excited.⁵¹ Since the same also holds for the projectile ^{48}Ti (going to ^{47}Sc and back to ^{48}Ti [see Ref. 52 for the reaction $^{45}\text{Sc}(^3\text{He}, d)^{46}\text{Ti}$]), we expect that after step 2' about 10 MeV has been converted to excitation energy, divided in equal parts between projectiles and target. Similarly, more complicated states (e.g., two-particle, one-hole states in $A+1$) can be populated as shown schematically in Fig. 21. Thus the deep-inelastic component of the experimental Q -value distributions shown in Fig. 20 consists of many contributions from multiparticle-multihole states in both reaction partners.

F. A random-walk model for deep-inelastic scattering

In this section we shall develop a more quantitative description of the model outlined in the last paragraph. As can be seen from Fig. 21 the first excited state in the nucleus $A+1$ can be reached via different routes (1-2-3' and 1-2'-3''), where each step n has to be weighted with the probability Q_n that an n -step reaction actually occurs. Since transfer can occur along the neutron and the proton axis, this leads to a description of the whole process as a two-dimensional random walk on a N - Z lattice. Denoting the one-step displacement vectors on this lattice $(\Delta N, \Delta Z) = (0, 1), (1, 0), (0, -1), (-1, 0)$ and including inelastic scattering with $(0, 0)$ by $\Delta_i, i=0, 4$, then the probability distribution $P_n(N, Z)$ after n steps is related to the probability P_{n-1} after $n-1$ steps by (see Ref. 53)

$$P_n(N, Z) = Q_n \sum_{i=0}^4 P_{n-1}[(N, Z) - \Delta_i] \times T_i[(N, Z) - \Delta_i], \quad (7)$$

where $T_i[(N, Z) - \Delta_i]$ are the properly normalized transition probabilities for $[(N, Z) - \Delta_i] \rightarrow (N, Z)$. Equation (7) is identical to the one used in Ref. 53, except that each step n is weighted with the probability Q_n that during the interaction time an n -step interaction occurred. These weighting factors, which have been neglected in previous

random-walk calculations^{53,54} will be given below. If in addition a prescription for calculating T_i is given, the evolution of the transfer process from the initial condition $P_0(N, Z) = \delta(N, N_0)\delta(Z, Z_0)$ can be calculated.

Each step in the random walk is associated with an energy loss which, as discussed in Sec. IV E, is about 10 MeV for the two-step route 1-2'. Similar values have been obtained from a study of lighter systems by Mikumo *et al.*²⁹ who deduced an energy loss in each transfer process of

$$\Delta Q = -0.1(E_i - V_c^i) - 0.9 \quad (8)$$

for $n \leq 4$ and

$$\Delta Q' = -0.061(E_i - V_c^i) + 0.11 \quad (9)$$

for $n > 4$. E_i and V_c^i in Eqs. (8) and (9) are the c.m. energy and the Coulomb potential in the entrance channel, respectively. For the system $^{48}\text{Ti} + ^{208}\text{Pb}$, one calculates $\Delta Q = -6.38$ MeV and $\Delta Q' = -3.23$ MeV which is of the same magnitude as the rough estimate given above.

With an energy loss per particle as given by Eqs. (8) and (9) and the underlying driving potential of Eq. (5), one is able to generate Q -value spectra from the solution of Eq. (7) and compare them with experimental data.

For the transition probability T_i two different assumptions have been made. (i) Each step is equally probable. This leads to a symmetric Gaussian distribution for the resulting (N, Z) spectrum. Such behavior has been found for many reactions induced by heavy projectiles (see, e.g., Ref. 3). (ii) The transition probability is determined by the level density of the final state reached with the particle transfer of type Δ_i (see Ref. 53). This assumption strongly favors transfers which lead toward the bottom of the valley of the driving potential in Fig. 18. Such behavior of the transfer probability is well known from light heavy-ion induced transfer reactions, e.g., $^{16}\text{O} + ^{208}\text{Pb}$ (see Ref. 31).

At this point, some of the advantages of a random-walk description for the multiparticle transfers, as compared to, for example, diffusion-type models,⁴⁴ should be mentioned. (i) The structure of Eq. (7) allows the use of different transition probabilities for different reaction steps n in order to investigate if, for example, the entrance phase is governed by phase-space considerations while in later stages a stochastic exchange of protons and neutrons occurs. (ii) Complicated nonanalytic driving potentials (see Fig. 18) can easily be incorporated in a random-walk description of the nucleon transfer. (iii) Before each step in the random walk, it is checked if this particular transfer is energetically allowed. If all available energy is dissipated, the random walk stops. Thus energy conservation is automatically included in the model. This feature is particularly important at energies in the vicinity of the Coulomb barrier.

The conditions under which the random-walk model and the diffusion model are equivalent have been discussed in Ref. 55. The main difference between previous random-walk descriptions of nucleon transfer^{53,56-58} and Eq. (7) are the probabilities Q_n , which take into account that each step in the random-walk chain has to be weighted with the probability that an n -step process actu-

ally occurs. Moreover, the normalized yield for all isotopes generated in this random walk has to be equal to the cross section for all transfer reactions generated during the interaction.

The probability for the occurrence of an n -step process was calculated using the perturbative statistical model developed by Tanabe.⁵⁹ The probability Q_n is given by a Poisson distribution

$$Q_n(D) = \frac{S(D)^n}{n! \exp[S(D)]} \quad (10)$$

with

$$S(D) = \frac{2}{v} W(D) \frac{\sqrt{2\pi a D}}{h}, \quad (11)$$

where D is the distance of closest approach, $W(D)$ the imaginary potential at this distance, and a the diffuseness of the potential. With the potential parameters used in the coupled-channels calculations (see Sec. IV A), we obtain $Q_n(D)$ for $n = 1-10$ as shown in Fig. 22. As can be seen, the probability for a one-step reaction is largest for grazing-type collisions and peaks at a distance of about 14 fm, close to the value obtained for the one-neutron transfer reaction (see Fig. 16). For more central collisions, multistep reactions start to dominate the reaction mechanism. Since the model calculations will be compared with angle integrated Q -value spectra, the Q_n factors of Eq. (7) correspond to the area under the $Q_n(D)$ distributions shown in Fig. 22. With $Q_n(D)$ given by Eqs. (10) and (11), the random-walk problem can be solved without any free parameters, since the total transfer yield calculated using Eq. (7) has to equal the measured integrated transfer cross sections for all outgoing channels.

The experimental data (see Figs. 10 and 11) do not support either of the assumptions made above for the transition probability T_i . The experimental cross section for the production of V and Cr isotopes is very low, which is at variance with the assumption of equal transition probability for transfers in all directions. The level density

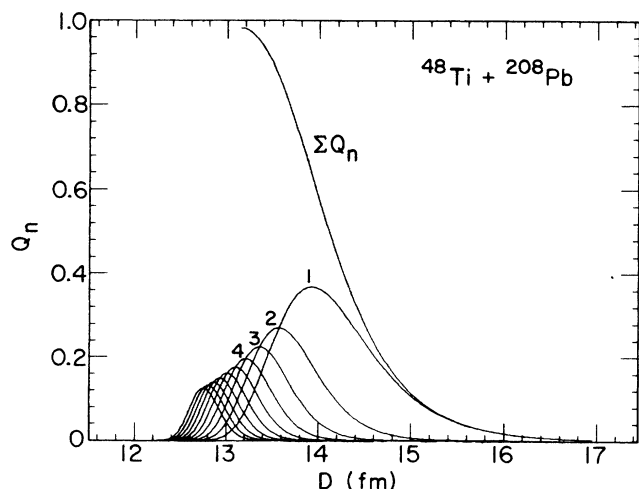


FIG. 22. Probability for the occurrence of an n -step reaction in the system $^{48}\text{Ti} + ^{208}\text{Pb}$ plotted as a function of the distance of closest approach D . (See text for details).

alone also cannot be the only determining factor for T_i , since it would strongly favor the production of neutron-rich Ti, Sc, and Ca isotopes which is also not observed experimentally. Neutron evaporation (which is of the order of about 1 neutron for $Q = -60$ MeV) does not alter this conclusion. We have therefore calculated the production cross section for several isotopes in the vicinity of ^{48}Ti , under the assumption that only the first n steps of the interaction are governed by the underlying phase space, while starting with step $(n+1)$ a stochastic exchange of protons and neutrons occurs with equal probability for all directions. The results are shown in Fig. 23, where the cross sections for the production of several nuclei (explained in the figure) are plotted as function of the step number r , where r is the step number from which a particle transfer occurs with equal probability in all directions. In the calculations the level density parameter was taken as $a = A/8$ (where A is the total mass of the system), and a probability of 20% for inelastic excitation was assumed. The choice of these parameters does not critically influence the conclusions stated above. As can be seen from Fig. 23, the asymmetry in the mass flow, which strongly favors the production of ^{49}Ti over ^{47}Ti , is caused by the effect of the driving potential. If proton and neutron exchange occurs with equal probability, the production cross sections for $^{47,49}\text{Ti}$, ^{47}Sc , and ^{49}V (not shown) are identical ($r=1$). If the first step is governed by the driving potential and stochastic exchange starts with the second step ($r=2$), a large asymmetry is obtained. This asymmetry persists if the random exchange starts at even later stages. In these cases, however, a strong preference for the formation of neutron-rich isotopes (shown for the example of ^{50}Ti) is obtained, which is at variance with the experiment. From a comparison with the experimental cross sections we therefore conclude that only the first one or two steps of the interaction are governed by the driving potential, while in the later stages a random exchange of protons and neutrons in both directions occurs.

Figure 24 shows a comparison of the measured Q -value

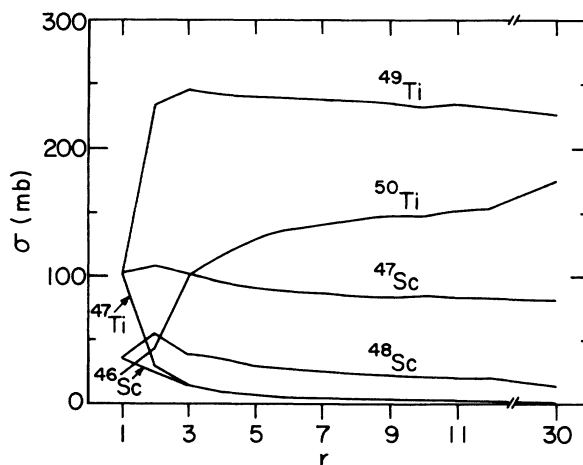


FIG. 23. Cross sections for the production of several isotopes in the vicinity of ^{48}Ti plotted vs the step number r from which random exchange of particles occurs (see text for details).

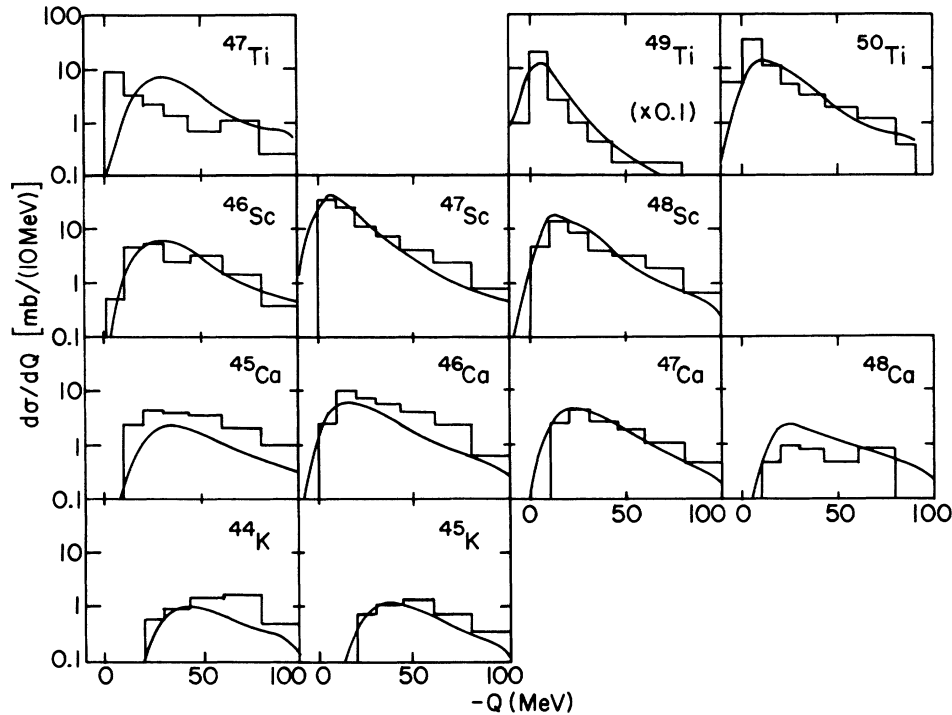


FIG. 24. Measured Q -value spectra (histograms) and theoretical predictions (solid lines) for several reaction channels from the interaction of $^{48}\text{Ti} + ^{208}\text{Pb}$ at $E_{\text{lab}} = 300$ MeV.

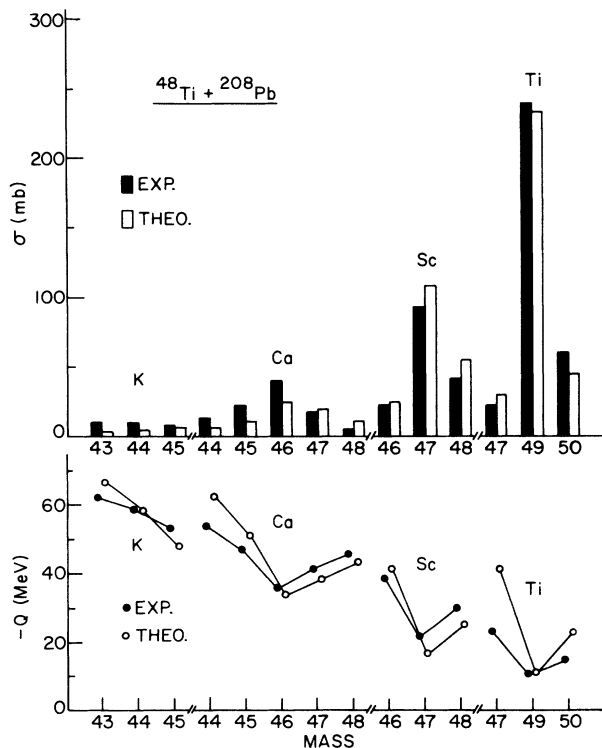


FIG. 25. Comparison of experimental data and theoretical predictions for integrated cross sections and average Q values for several reaction channels from the reaction $^{48}\text{Ti} + ^{208}\text{Pb}$ at $E_{\text{lab}} = 300$ MeV.

spectra (obtained from projections of the Wilczyński plots), shown as histograms, with the results obtained from Eq. (7) (solid lines). The stochastic exchange starts at $r = 2$ in these calculations. In order to obtain a smooth energy spectrum, the theoretical distributions were folded with a Gaussian of variance $\sigma^2 = 40$ MeV². The agreement is generally quite good, both in absolute magnitude and in the shape of the energy spectra. This is further emphasized in Fig. 25, where the energy integrated cross sections and the average Q values of the energy spectra are compared. The average Q values in particular are remarkably well reproduced. For neutron-deficient reaction products which lie far away from the starting nucleus ^{48}Ti (e.g., ^{44}Ca , ^{44}K , ^{43}K), the theory predicts smaller cross sections than observed experimentally which emphasizes the fact that experimentally only secondary reaction products are measured, favoring the more neutron-deficient isotopes within a given element.

The results obtained from this comparison suggest that, similar to reactions induced by lighter heavy ions (e.g., ^{16}O), the driving potential plays an important role in the entrance phase of the reaction. The driving potential causes a shift of the centroids of the charge and mass distributions towards lower Z and larger N . Only recently high-resolution experiments have made it possible to observe this shift. Starting from the second or third step, the interaction of the two nuclei is already strong enough so that the driving potential is of minor importance, and neutrons and protons are exchanged with equal probability. For ^{16}O induced reactions at similar energies above

the Coulomb barrier, these multistep reactions are associated with large negative Q values and lead to fusion (possibility followed by fission). It is the absolute value of the energy above the Coulomb barrier (which is larger in the case of $^{48}\text{Ti} + ^{208}\text{Pb}$) together with the large- l values of the reaction that make these multistep processes observable as deep-inelastic reactions.

V. SUMMARY

We have studied transfer reactions in the $^{46,48,50}\text{Ti} + ^{208}\text{Pb}$ systems at incident energies slightly above the Coulomb barrier with single mass and charge resolution. About $\frac{2}{3}$ of the total reaction cross section (not including inelastic scattering) is contained in these transfer reactions while about $\frac{1}{3}$ is due to fusion-fission processes. Quasi-elastic and deep-inelastic processes occur with about equal probability in the Ti + Pb reactions, allowing a detailed study of the correlations between the two reaction modes. The quasi-elastic transfer reactions are dominated by neutron-transfer processes. The neutron-transfer cross section is about 20% of the total reaction cross section. Deep-inelastic collisions, on the other hand, are spread over a much larger number of reaction channels with smaller individual contributions. The angular distributions consist of two components: a Gaussian component peaked at the grazing angle which is associated mainly with quasi-elastic events, and a forward-peaked (exponential) component, which gains its main contributions from deep-inelastic events. Wilczyński plots for individual transfer channels have been generated, showing that there is a *gradual* transition from quasi-elastic channels (prevalent for transfer products in the vicinity of the projectile) to deep-inelastic collisions which dominate the multiparticle-transfer reactions leading to products which are in the N - Z plane located far away from the projectile.

In the projection of the Wilczyński plots for various reaction channels onto the Q axis, again two components (quasi-elastic and deep-inelastic) are observed. The centroids for both components move to more negative Q

values with increasing charge transfer. The centroids of the low- Q (quasi-elastic) component plotted as function of the charge of the outgoing particle are in good agreement with the predictions from semiclassical kinematic matching conditions (Q -matching). The more negative- Q (deep-inelastic) component is in a simple model attributed to multiparticle-multihole excitations in the two outgoing nuclei. The strength of the various transfer reaction shows a strong asymmetry in the transfer direction favoring neutron-pickup and proton-stripping reactions. These yields and the structure of the Q -value spectra for various channels have been analyzed in a model which is based on a random walk in the N - Z plane. In this model it is easy to incorporate microscopic driving potentials based on actual masses for the nuclei involved. Energy conservation is checked for each transfer step which is an important factor for the reaction flow particularly at incident energies close to the Coulomb barrier. From a comparison with experimental cross sections, it is observed that different rules for the transfer probability exist for the entrance phase of the reaction, when the overlap of the two nuclei is still small, compared to the later stages when the transfer window is wide open. In the first one or two transfer steps, the available phase space (strongly influenced by the driving potential) dominates the transfer probability, while in the later phase of the reaction, when the nuclear overlap is larger, proton and neutron transfer occur with equal probability in all directions (subject to energy conservation).

ACKNOWLEDGMENTS

We want to thank the ATLAS accelerator crew for providing us with the stable Ti beams for this experiment. Discussions with H. Esbensen, S. Landowne, and S. C. Pieper are also gratefully acknowledged. This work was supported by the U. S. Department of Energy, Nuclear Physics Division, under Contract No. W-31-109-ENG-38 and by the U. S. National Science Foundation under Grant No. PHY84-16025.

*Present address: Fysisch Laboratorium, Rijksuniversiteit Utrecht, The Netherlands.

†Permanent address: University of Notre Dame, Notre Dame, IN 46556.

‡Present address: University of Mainz, West Germany.

§Present address: 26-415, Massachusetts Institute of Technology, Cambridge, MA 02139.

¹S. Landowne and A. Vitturi, in *Treatise on Heavy Ion Science*, edited by D. A. Bromley (Plenum, New York, 1985), Vol. 1, and references cited therein.

²R. J. Ascutto and E. A. Seglie, in *Treatise on Heavy Ion Science*, edited by D. A. Bromley (Plenum, New York, 1985), Vol. 1, and references cited therein.

³W. U. Schröder and J. R. Huizenga, in *Treatise on Heavy Ion Science*, edited by D. A. Bromley (Plenum, New York, 1985), Vol. 2, and references cited therein.

⁴D. Schüll, W. C. Shen, H. Freiesleben, R. Bock, R. Busch, D.

Bangert, W. Pfeffer, and F. Pühlofer, *Phys. Lett.* **102B**, 116 (1981).

⁵K. E. Rehm, D. G. Kovar, W. Kutschera, M. Paul, G. Stephans, and J. L. Yntema, *Phys. Rev. Lett.* **51**, 1426 (1983).

⁶S. Pontoppidan, P. R. Christensen, O. Hansen, F. Videbaek, H. C. Britt, B. H. Erkill, L. Patin, R. H. Stokes, M. P. Webb, R. L. Ferguson, F. Plasil, and G. R. Young, *Phys. Rev. C* **28**, 2299 (1983).

⁷W. von Oertzen, B. Gebauer, H. G. Bohlen, F. Busch, and D. Schüll, *Z. Phys. A* **313**, 189 (1983).

⁸H. Breuer, A. C. Mignerey, V. E. Viola, K. L. Wolf, J. R. Birkelund, D. Hilscher, J. R. Huizenga, W. U. Schröder, and W. W. Wilcke, *Phys. Rev. C* **28**, 1080 (1983).

⁹C. Brendel, J. Carter, F. Beck, A. Richter, G. Schrieder, D. Schüll, G. Delic, and R. H. Lemmer, *Phys. Lett.* **124B**, 474 (1983).

¹⁰A. H. Baltz, P. D. Bond, O. Hansen, J. Cheng-Lie, P. R.

- Christensen, S. Pontoppidan, F. Videbaek, D. Schüll, S. Wen-Quing, and H. Freiesleben, *Phys. Rev. C* **29**, 2392 (1984).
- ¹¹K. Sapotta, R. Bass, V. Hartmann, N. Noll, R. E. Renfordt, and K. Stelzer, *Phys. Rev. C* **31**, 1297 (1985).
- ¹²K. E. Rehm, A. van den Berg, J. J. Kolata, D. G. Kovar, W. Kutschera, G. Rosner, G. S. F. Stephans, J. L. Yntema, and L. L. Lee, *Suppl. J. Phys. Soc. Jpn.* **54**, 410 (1985).
- ¹³J. Wilczyński, *Phys. Lett.* **47B**, 484 (1973).
- ¹⁴J. L. Yntema and P. J. Billquist, *Nucl. Instrum. Methods* **199**, 637 (1982).
- ¹⁵J. L. Yntema and P. J. Billquist, *Nucl. Instrum. Methods* **220**, 107 (1984).
- ¹⁶J. R. Erskine, T. H. Braid, and J. G. Stoltzfus, *Nucl. Instrum. Methods* **135**, 67 (1976).
- ¹⁷Y. Baudinet-Robinet, *Nucl. Instrum. Methods* **190**, 197 (1981).
- ¹⁸A. Gavron, *Phys. Rev. C* **21**, 230 (1980); Y. Eyal and M. Hillman (unpublished).
- ¹⁹H. Sohlbach, H. Freiesleben, P. Braun-Munzinger, W. F. W. Schneider, D. Schüll, B. Kohlmeyer, M. Marinescu, and F. Pühlhofer, *Phys. Lett.* **153B**, 386 (1985).
- ²⁰R. Bock, Y. T. Chu, M. Dakowski, A. Gobbi, E. Grosse, A. Olmi, H. Sann, D. Schwalm, U. Lynen, W. Müller, S. Bjornholm, H. Esbensen, W. Wölfl, and E. Morenzi, *Nucl. Phys.* **A388**, 334 (1982).
- ²¹K. E. Rehm, F. L. H. Wolfs, A. M. van den Berg, and W. Henning, *Phys. Rev. Lett.* **55**, 280 (1985).
- ²²M. H. Macfarlane and S. C. Pieper, Argonne National Laboratory Report No. ANL-76-11 (Ref. 1), 1978 (unpublished).
- ²³R. L. Auble, *Nucl. Data Sheets* **24**, 1 (1978).
- ²⁴J. R. Beene, *Nucl. Data Sheets* **23**, 1 (1978).
- ²⁵D. E. Alburger, *Nucl. Data Sheets* **42**, 369 (1984).
- ²⁶A. M. R. Joye, A. M. Baxter, M. P. Fewell, D. C. Kean, and R. H. Spear, *Phys. Rev. Lett.* **38**, 807 (1977).
- ²⁷W. E. Frahn, *Nucl. Phys.* **A302**, 267 (1978).
- ²⁸U. Brosa and W. Westmeier, *Nucl. Phys.* **A441**, 109 (1985).
- ²⁹T. Mikumo, M. Sasagase, M. Sato, T. Ooi, T. Higashi, Y. Nagashima, and M. Yamanouchi, *Phys. Rev. C* **21**, 620 (1981).
- ³⁰K. E. Rehm, GSI Report No. GSI-86-19 1986 (unpublished), p. 129.
- ³¹F. Videbaek, R. B. Goldstein, L. Grodzins, S. G. Steadman, T. A. Belote, and J. D. Garrett, *Phys. Rev. C* **15**, 954 (1977).
- ³²R. Bass, *Nuclear Reactions with Heavy Ions* (Springer, Berlin, 1980), and references cited therein.
- ³³H. Feldmeier, in *Nuclear Structure and Heavy Ion Dynamics*, edited by L. Moretto and R.A. Ricci (North-Holland, Amsterdam, 1984), p. 274.
- ³⁴M. Lefort and Ch. Ngo, *Ann. Phys.* **3**, 5 (1978).
- ³⁵J. R. Huizenga, W. U. Schröder, J. R. Birkelund, and W. W. Wilcke, *Nucl. Phys.* **A387**, 257 (1982).
- ³⁶J. J. Kolata, K. E. Rehm, D. G. Kovar, G. S. Stephans, G. Rosner, H. Ikezoe, and E. Vojtech, *Phys. Rev. C* **30**, 125 (1984).
- ³⁷A. M. van den Berg, W. Henning, L. L. Lee, K. T. Lesko, K. E. Rehm, J. P. Schiffer, G. S. F. Stephans, and F. L. H. Wolfs, *Phys. Rev. C* **37**, 178 (1988).
- ³⁸A. G. Artukh, V. V. Avdeichikov, J. Erö, G. F. Gridnev, V. L. Mikheev, V. V. Volkov, and J. Wilczyński, *Nucl. Phys.* **A160**, 511 (1971).
- ³⁹S. C. Pieper, M. H. Macfarlane, D. H. Gloeckner, D. G. Kovar, F. D. Bechetti, B. G. Harvey, D. K. Hendrie, H. Homeyer, J. Mahoney, F. Pühlhofer, W. von Oertzen, and M. S. Zisman, *Phys. Rev. C* **18**, 180 (1978).
- ⁴⁰M. L. Halbert, *Nucl. Data Sheets* **24**, 175 (1978).
- ⁴¹A. M. van den Berg, K. E. Rehm, D. G. Kovar, W. Kutschera, and G. S. F. Stephans, *Phys. Lett. B* **194**, 334 (1987).
- ⁴²H. Siekmann, B. Gebauer, H. G. Bohlen, H. Kluge, W. von Oertzen, P. Fröbrich, B. Strack, K. D. Hildenbrand, H. Sann, and U. Lynen, *Z. Phys. A* **307**, 113 (1982).
- ⁴³W. von Oertzen, H. G. Gebauer, R. Künkel, F. Pühlhofer, and D. Schüll, *Z. Phys. A* **326**, 465 (1987).
- ⁴⁴H. A. Weidenmüller, in *Progress in Particle and Nuclear Physics*, edited by D. Wilkensen (Pergamon, New York, 1980), Vol. 3, p. 49.
- ⁴⁵W. Bohne, P. Fröbrich, K. Grabisch, K. Hartmann, H. Lehr, H. Morgenstern, and W. Stöffer, *Z. Phys. A* **313**, 19 (1983).
- ⁴⁶D. K. Locke, R. Vandenbosch, and A. Lazzarini, *Nucl. Phys.* **A384**, 241 (1982).
- ⁴⁷M. Marinescu, D. Bangert, B. Kohlmeyer, F. Pühlhofer, W. F. W. Schneider, D. Schüll, H. Freiesleben, and H. Sohlbach, GSI Annual Report No. GSI-84-1, 1983 (unpublished).
- ⁴⁸A. H. Wapstra and K. Bos, *At. Data Nucl. Data Tables* **17**, 474 (1976).
- ⁴⁹J. J. Griffin and W. Broniowski, *Nucl. Phys.* **A428**, 143 (1984).
- ⁵⁰P. J. A. Buttle and L. J. B. Goldfarb, *Nucl. Phys.* **A176**, 299 (1971).
- ⁵¹E. A. McClatchie, C. Glashauser, and D. L. Hendrie, *Phys. Rev. C* **1**, 1828 (1970).
- ⁵²L. Broman and D. J. Pullen, *Nucl. Phys.* **A110**, 161 (1968).
- ⁵³J. J. Griffin, J. Bonch, M. Dworzecka, and K.-K. Kan, *Nucl. Phys.* **A369**, 181 (1981).
- ⁵⁴A. Gökmén, M. Dworzecka, and J. J. Griffin, *Nucl. Phys.* **A440**, 586 (1985), and references therein.
- ⁵⁵J. M. Akkermans, *Z. Phys. A* **313**, 83 (1983).
- ⁵⁶D. Bangert, B. Kohlmeyer, M. Marinescu, F. Pühlhofer, F. Busch, and D. Schüll, GSI Annual Report No. GSI-83-1, 1982 (unpublished).
- ⁵⁷G. Rudolf, *Z. Phys. A* **320**, 325 (1985).
- ⁵⁸J. Toke and A. Gobbi, GSI Annual Report No. GSI-82-1, 1981 (unpublished).
- ⁵⁹H. Tanabe, *Nucl. Phys.* **A423**, 139 (1984).